BIOMEDICAL MATERIALS

A method for single-neuron chronic recording from the retina in awake mice

Guosong Hong[1]*, Tian-Ming Fu[1]*, Mu Qiao[2]*, Robert D. Viveros[3], Xiao Yang[1], Tao Zhou[1], Jung Min Lee[1,4], Hong-Gyu Park[1,4], Joshua R. Sanes[2], Charles M. Lieber[1,3]†

The retina, which processes visual information and sends it to the brain, is an excellent model for studying neural circuitry. It has been probed extensively ex vivo but has been refractory to chronic in vivo electrophysiology. We report a nonsurgical method to achieve chronically stable in vivo recordings from single retinal ganglion cells (RGCs) in awake mice. We developed a noncoaxial intravitreal injection scheme in which injected mesh electronics unrolls inside the eye and conformally coats the highly curved retina without compromising normal eye functions. The method allows 16-channel recordings from multiple types of RGCs with stable responses to visual stimuli for at least 2 weeks, and reveals circadian rhythms in RGC responses over multiple day/night cycles.

As an approachable part of the brain, the retina provides an excellent model for analyzing the assembly and function of information-processing circuits in the central nervous system (CNS) (*1*, *2*). Interneurons receive signals from light-sensitive photoreceptors (rods and cones) and pass it to retinal ganglion cells (RGCs), which send axons through the optic nerve to visual areas of the brain. Whereas photoreceptors are akin to pixels, information processing by interneurons renders each of ≥40 types of RGCs selectively responsive to specific visual features such as motion or color contrasts (*2*–*4*). However, whereas in vivo single-neuron recordings in awake, behaving animals are routine for many parts of the brain (*5*, *6*), analysis of RGCs has relied primarily on ex vivo electrophysiological recording (*7*, *8*) and calcium imaging (*4*). Although these ex vivo studies have provided deep insights into retinal computations, they are limited in several respects. First, systemic effects such as neuromodulation, alterations in hormonal milieu, and circadian variation are difficult to study ex vivo (*9*–*12*). Second, recordings are limited to the short lifetime of the preparation, typically a few hours, so their ability to detect plasticity in activity patterns is compromised. Third, rod function is prone to rapid loss in explants, partly because of its dependence on pigment epithelium, which is generally removed during explantation. Therefore, ex vivo recordings of rod activities over extended times have remained challenging (*4*). Finally, it is obviously infeasible to correlate retinal activity ex vivo with organismic responses or behaviors. In vivo RGC electrophysiology could offer insight into the interaction between the retina and related brain regions involved in vision processing and regulation (*9*, *13*–*15*), yet existing technologies either have been unable to achieve recordings at single-RGC resolution in mice (*11*) or have been limited to one or two channels of acute recording in anesthetized animals with larger eyes (*16*, *17*).

We report chronically stable in vivo recordings from functionally diverse RGCs in awake mice using epiretinal-implanted mesh electronics delivered via noncoaxial and minimally invasive intravitreal injection to form a chronically stable conformal retina interface. We designed a 16-channel mesh electronics probe with recording electrodes distributed evenly over a 1.5 mm × 0.8 mm region in four parallel rows to ensure coverage and interrogation of a large area of the retina after injection. The 16 recording electrodes (Fig. 1A, I, green arrow) are individually addressable through polymer-encapsulated metal interconnect lines that terminate at input/output (I/O) pads (Fig. 1A, I, red arrow), which provide connection to external recording instrumentation. The tissue-like mesh electronics probes were fabricated using standard photolithography (*18*–*22*), with ~90% porosity in two dimensions and mesh ribbon element widths of ≤10 μm to facilitate syringe injection through capillary needles and to minimize interference with the retina.

The three-dimensional highly concave mouse retina precludes using conventional methods, such as silicon, glass, or metal electrodes (*7*, *16*, *23*) or planar microelectrode arrays (*8*), to form a conformal and chronically stable retina interface.

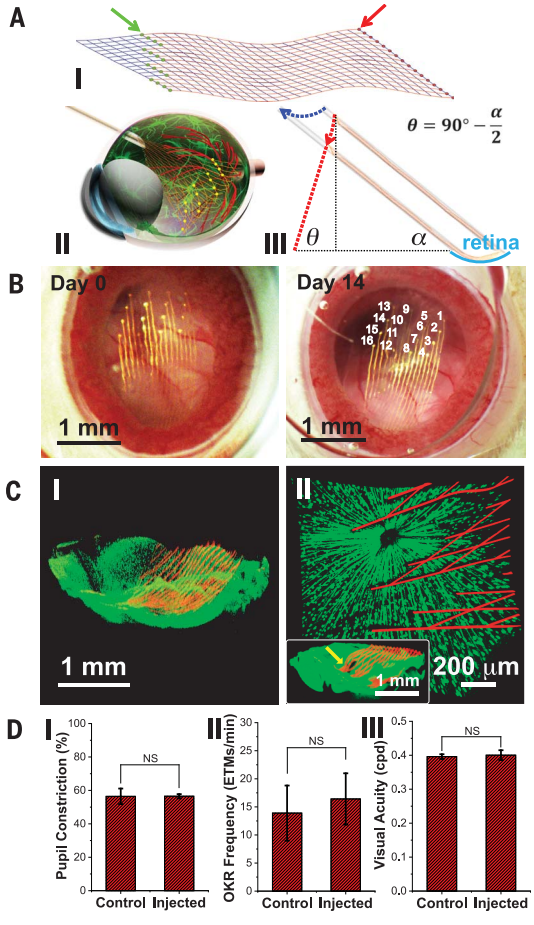

Fig. 1. Noncoaxial intravitreal injection and conformal coating of mesh electronics on the mouse retina. (**A**) I: Schematic showing the layout of mesh electronics comprising 16 recording electrodes (green dots indicated by a green arrow) and I/O pads (red dots indicated by a red arrow). II: Schematic showing noncoaxial intravitreal injection of mesh electronics onto the RGC layer. Multiplexed recording electrodes are shown as yellow dots. III: Schematic of noncoaxial injection that allows controlled positioning of mesh electronics on the concave retina surface (cyan arc). The blue and red dotted arrows indicate the motion of the needle and desired trajectory of the top end of the mesh, respectively (see fig. S1 for details) (*22*). (**B**) In vivo through-lens images of the same mouse eye fundus on days 0 and 14 after injection of mesh electronics, with electrode indexing in the day 14 image (*22*). (**C**) Ex vivo imaging of the interface between injected mesh electronics (red, mesh polymer elements) and the retina (green dots, RGCs) on days 0 (I) and 7 (II) after injection. The inset of II shows the region indicated by a yellow arrow where the high-resolution image was taken (*22*). (**D**) Comparison of pupillary reflex ($n = 3$), OKR ($n = 5$), and visual acuity ($n = 3$) between control and injected mouse eyes. Error bars denote SD; NS, not significant ($P > 0.05$) by one-way ANOVA test.

[1]Department of Chemistry and Chemical Biology, Harvard University, Cambridge, MA, USA. [2]Center for Brain Science and Department of Molecular and Cellular Biology, Harvard University, Cambridge, MA, USA. [3]John A. Paulson School of Engineering and Applied Sciences, Harvard University, Cambridge, MA, USA. [4]Department of Physics, Korea University, Seoul, Republic of Korea.
*These authors contributed equally to this work.
†Corresponding author. Email: cml@cmliris.harvard.edu

Therefore, we asked whether the unique unrolling/unfolding capability of mesh electronics in aqueous solutions (*19*) could occur in the vitreous humor of the eye, which has a very low Young's modulus (*24*). This scheme could enable delivery of a large mesh (>1 mm^2) through a much smaller nonsurgical injection hole (<0.1 mm^2). To deliver the mesh electronics into a mouse eye and form a conformal interface, we developed a controlled noncoaxial injection scheme (Fig. 1A, II and III) with several key features. First, the intravitreal injection procedure is compatible with standard stereotaxic frames commonly used for brain probe implantation (fig. S1, A and B). Second, the ultraflexibility of mesh electronics enables loading and controlled injection into the eye through the lateral canthus, using a small (outer diameter 330 μm) glass capillary needle (fig. S1B and fig. S2, A and B, blue arrows) that is similar in diameter to 29-gauge needles commonly used for intraocular injection of virus vectors and drugs (*25*). Third, synchronizing the volumetric flow with the lateral motion of the needle to follow the curvature of the retina affords lateral positioning and conformal coating of mesh electronics onto the concave retina surface (Fig. 1A, III, fig. S1C, and fig. S3). After injection and needle withdrawal, the mesh was glued externally (fig. S2, C and D) (*22*) and the I/O pads were connected to an interface cable (flexible flat cable), which was mounted on top of the skull, for electrical recording (*20*). The demonstrated injection of mesh electronics into the mouse eye represents a challenging case because of its small size and large curvature; we expect that this method could be readily adapted for animals with larger and less curved eyes, including nonhuman primates.

To verify that the mesh electronics, which is elastically strained when loaded into the capillary needle (*19*), unrolled from the capillary to cover the retina after noncoaxial intravitreal injection, we devised a method for noninvasive in vivo through-lens imaging based on a liquid Hruby lens (Fig. 1B and fig. S4) (*22*). Mesh electronics and retinal vasculature were both visualized from day 0 to day 14 after injection. Quantitative analysis of the locations of representative recording electrodes demonstrated minimal variation of electrode positions over 14 days (table S1) (*22*). We also performed confocal microscopic imaging of the mesh-retina interface after dissection of mesh-injected eyes from TYW3 transgenic mice in which a subset of RGCs was labeled with yellow fluorescent protein (YFP) (*26*) on day 0 and day 7 after injection. Images (Fig. 1C, I) (*22*) showed that the mesh conformed to the concave structure of the retina with a mean distance of 51 ± 35 μm (mean ± SD) between an electrode and the closest labeled RGC. Given that only 10% of RGCs are labeled in the TYW3 mouse retina (*27*), the nearest RGC is likely closer than this mean distance. Higher-resolution images (Fig. 1C, II) further showed that the average soma diameter of RGCs, 12.2 ± 1.9 μm (mean ± SD), was similar to the 10-μm width of mesh elements, and the density of labeled RGCs, 353 cells/mm^2, was within the reported range of 200 to 400 cells/mm^2

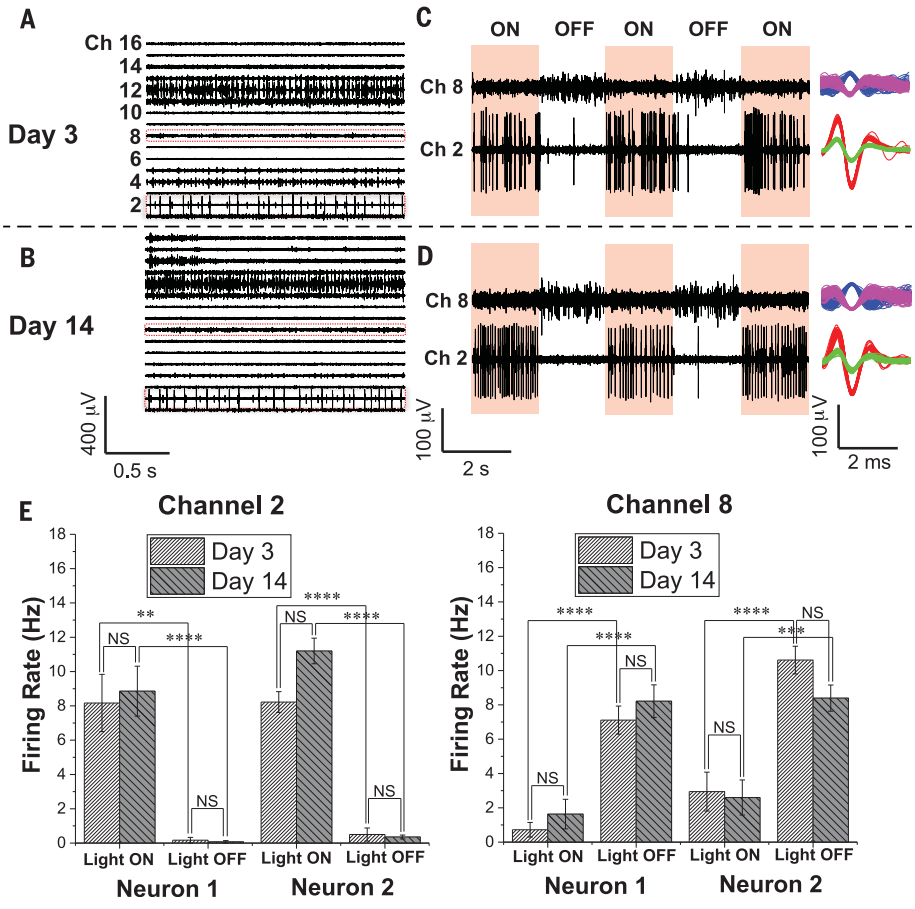

Fig. 2. Chronic 16-channel in vivo electrophysiology of single RGCs measured with mesh electronics. (**A** and **B**) Representative 16-channel recordings from the same mesh electronics delivered onto a mouse retina on day 3 (A) and day 14 (B) after injection. (**C** and **D**) Light modulation of two representative channels (Ch2 and Ch8) in red dashed boxes in (A) and (B) on day 3 (C) and day 14 (D) after injection. The red shaded and unshaded regions indicate the light ON and OFF phases, respectively. Representative sorted spikes assigned to different neurons on both days are shown in the rightmost column for each channel. Each distinct color in the sorted spikes represents a unique identified neuron. (**E**) Firing rates of all sorted neurons from Ch2 and Ch8 during light modulations on days 3 and 14 after injection (*22*). Error bars denote SEM. $^{**}P < 0.01$, $^{***}P < 0.001$, $^{****}P < 0.0001$ (one-way ANOVA); NS, not significant ($P > 0.05$). Five mice were used for multiplexed recordings.

for YFP-labeled RGCs in the central retina of TYW3 mice (*27*). Together, the in vivo and ex vivo images confirmed a chronically stable, conformal, and intimate interface between the three-dimensional curved retina and the injected mesh electronics, with no observable perturbation of RGC density or distribution.

Because of the rigidity of conventional probes used for single-channel in vivo retina recording in larger animals, sutures and fixation rings are usually used to suppress the normal motor functions of the eye even when the animals are anesthetized (*16*, *28*). We asked whether we could take advantage of the ultraflexibility of mesh electronics to minimize interference with normal eye functions during recording in awake mice. First, we used near-infrared imaging (*13*) to track eye responses during air puffs. Chronic studies of the blink reflex exhibited immediate and complete responses to timed air puffs (fig. S5A), with no statistically significant difference between mesh-implanted and control eyes (fig. S5C, I). Second, to assess retinal responsiveness to light, we measured the pupillary response as a function of ambient light intensity modulation for control eyes and mesh-injected eyes (fig. S5B and movie S1). We detected prompt and full-scale pupil expansion and shrinkage in response to increases and decreases in brightness, respectively (fig. S5C, II). Quantification of pupil constriction (*22*) revealed no statistically significant difference between control eyes and mesh-injected eyes (Fig. 1D, I). Third, to assess the influence of the injected mesh on normal eye movement, we characterized the optokinetic reflex (OKR) in response to moving gratings (*29*). We observed that the amplitude, temporal pattern, directionality, and speed of the OKR were consistent between the control and mesh-injected eyes (fig. S5D). Quantitative analyses of eye movement frequency showed no statistically significant difference between the mesh-injected and control eyes

(Fig. 1D, II), both of which were also consistent with previous reports (*30*). Last, to evaluate the impact of the injected mesh on visual acuity, we measured the OKR in response to moving gratings with varying spatial frequencies, and found the mesh-injected eyes to exhibit the same visual acuity as the control (~0.4 cycles per degree; Fig. 1D, III) (*31*). It is also noteworthy that the transparent polymer constituting the mesh scaffold with <5% space occupied by metal features yields minimal blockage of incoming light, as evidenced by the ~95% light transmittance in the 400- to 600-nm spectral window visible to the mouse (*32*) (fig. S5C, II, inset), resulting in negligible distortion of visual input. Taken together, these data demonstrate that injection of the mesh electronics causes minimal damage to the orbicularis oculi, iris dilator, and extraocular muscles as well as negligible interference with light perception and visual acuity of the retina.

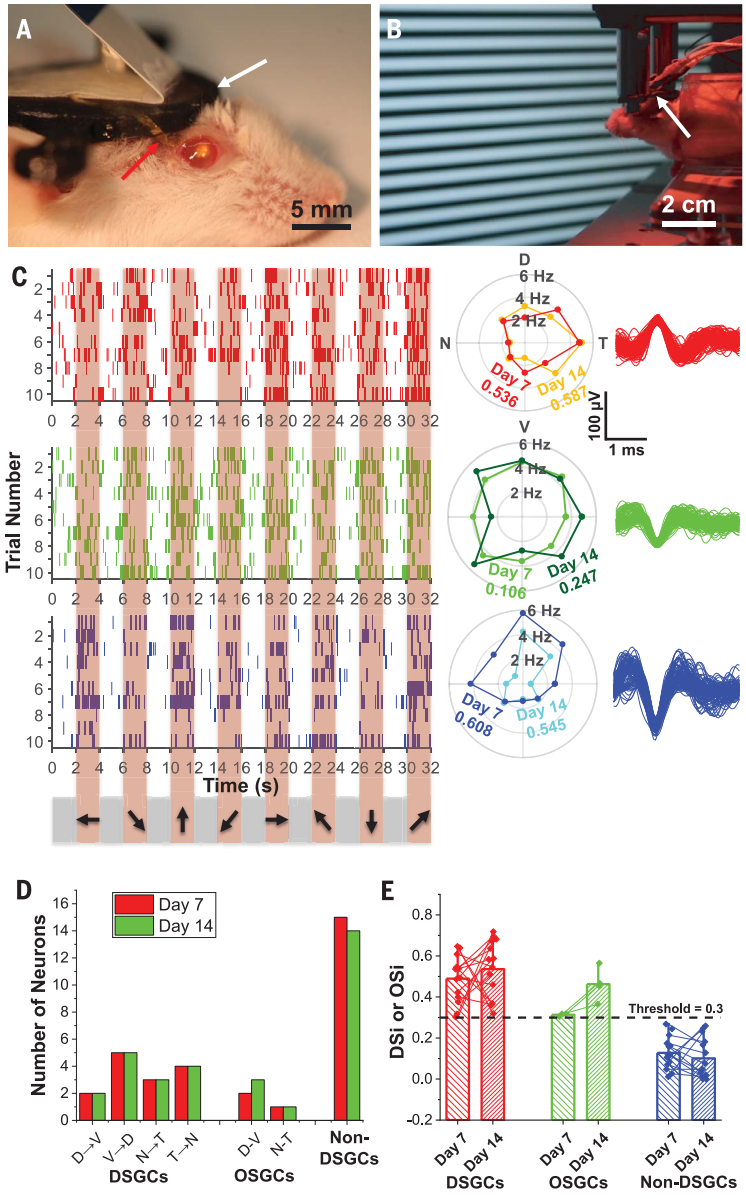

Fig. 3. Chronic in vivo recording and tracking of the same DSGCs. (**A**) Photograph showing a mouse immediately after mesh injection. The red and white arrows indicate part of mesh electronics outside of the eye and a head plate for head fixation, respectively. (**B**) Red-light photograph showing in vivo recording of DSGCs in response to moving grating stimulations (*22*). (**C**) Raster (left), polar plots (center), and overlaid spike waveforms (right) of single-unit firing events of three neurons (with corresponding colors) from Ch8 in response to moving grating stimulations on days 7 and 14 after injection. In the raster plots, the pink shaded regions correspond to times when gratings were displayed on the screen, with moving directions indicated by arrows on the bottom (*22*). Only the raster plots on day 7 are shown. In the polar plots, the DSi for each cell on different days is labeled with corresponding colors. (**D**) Bar chart summarizing numbers of identified DSGCs, OSGCs, and non-DSGCs on day 7 (red bars) and day 14 (green bars) after injection. (**E**) Bar chart with overlaid scatterplot of DSi or OSi of all RGCs on days 7 and 14, with thin lines of corresponding colors connecting the same neurons identified on both days. The bar height and the whisker indicate the mean and maximum of DSi and OSi values, respectively. Four mice were used for direction and orientation selectivity studies; data shown are from one representative mouse.

Having shown that the mesh electronics probe has negligible effect on normal visual functions, we conducted a series of tests to investigate its ability to detect the diverse RGC activities. First, we asked how many of the 16 channels in the implanted probe were sufficiently close to RGCs to record single-unit activity. Figure 2A and fig. S6A show examples from two mice in which we obtained high-quality recordings from all 16 channels, with a signal-to-noise ratio (SNR) of >7 for single-unit spikes. Moreover, single-unit activity was detected in at least 12 channels from each of five separate mice, thus highlighting the robustness of the injected probes for multiplexed retinal electrophysiology.

Second, we asked whether we could record repeatedly from the same sets of RGCs. Multiplexed 16-channel recordings revealed that the SNR from all channels remained >7 for single-unit spikes on days 3 and 14, with little variation in SNR for each specific channel (Fig. 2, A and B, and fig. S7A). The ON/OFF light response in these two representative channels (Ch2 and Ch8; Fig. 2, C and D), which included four RGC neurons (two for each channel) identified by spike sorting, also demonstrated statistically significant differences in modulation of firing patterns (Fig. 2E). Specifically, analysis of variance (ANOVA) showed a statistically significant ($P < 0.01$) difference in firing rate between ON and OFF phases of light modulation, but no significant ($P > 0.05$) difference during the same ON or OFF phase at different days (*22*). Furthermore, analyses of the ON-OFF indices (*4*, *22*) yielded values of 0.97 and 0.91 for the two Ch2 neurons and –0.74 and –0.55 for the two Ch8 neurons; thus, the two Ch2 and two Ch8 neurons can be identified as ON and OFF RGCs, respectively.

Third, we asked whether it was possible to assess the chronic stability and behavior of individual RGCs. We implemented a spike sorting protocol to identify and cluster single units based on principal components analysis (PCA) (*22*, *33*). L-ratio analysis (table S2) (*34*) together with characterization of the number and spike waveforms of detected neurons from all 16 channels on days 3 and 14 (fig. S7B) indicated good unit separation and chronic recording stability. Furthermore, systematic characterization from the two representative channels (Ch2 and Ch8; Fig. 2, C and D, right column) from day 0 through day 14 showed similar average spike waveforms indicative of chronic recording stability (fig. S8A). Moreover, quantitative waveform autocorrelation analyses (fig. S8B) (*35*) showed that the same four neurons were stably tracked across this period. Together, we isolated 134 single units from 89 channels

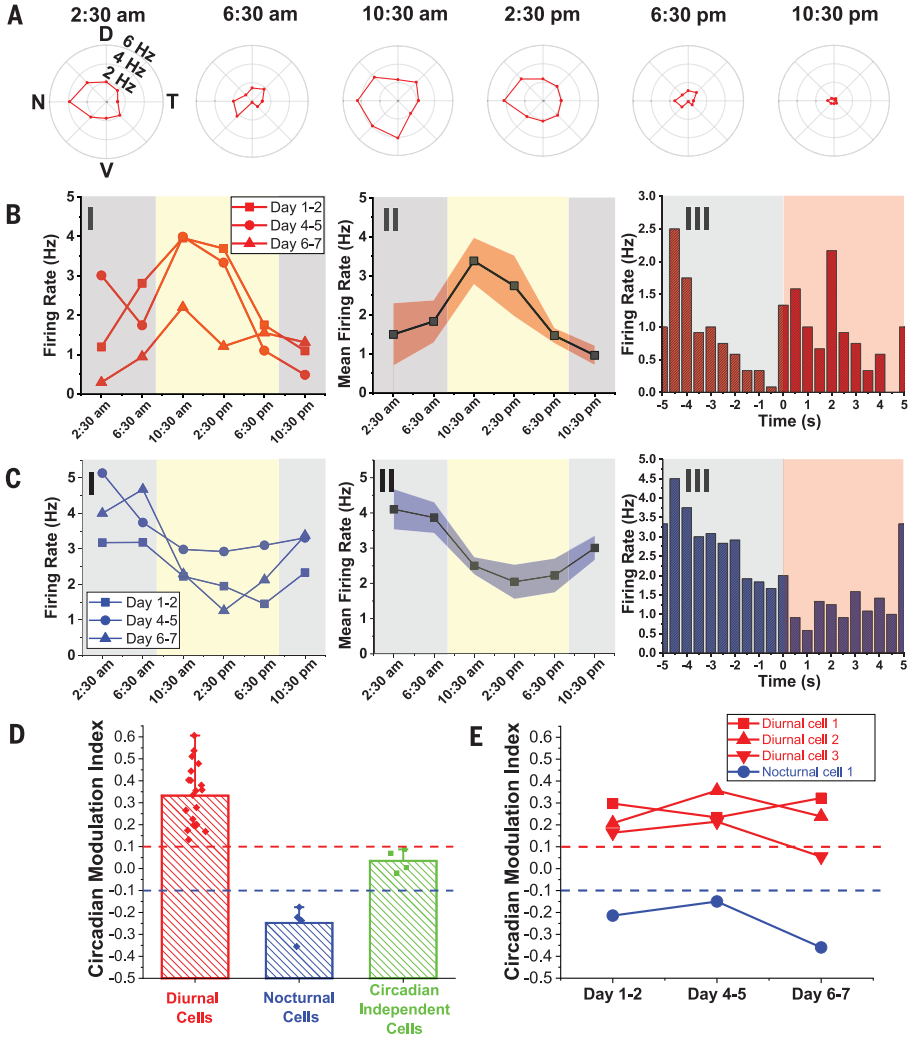

Fig. 4. Chronic circadian modulation of individual RGC activity. (**A**) Representative polar plots of a DSGC at different times in one complete circadian cycle on days 4 and 5 after injection. All graphs are plotted in same range of firing frequencies. (**B**) I: Firing rates of the same DSGC in (A) averaged over preferred directions in three complete circadian cycles on days 1 and 2, 4 and 5, and 6 and 7 after injection. II: Mean firing rate by taking the average over these three circadian cycles. III: This DSGC is identified as an ON-OFF transient type. (**C**) I: Firing rates of another DSGC averaged over preferred directions on three complete circadian cycles on days 1 and 2, 4 and 5, and 6 and 7 after injection. II: Mean firing rate by taking the average over these three circadian cycles. III: This DSGC is identified as an OFF transient type. In (B) and (C), I and II, yellow and gray shaded regions indicate diurnal and nocturnal circadian times, respectively; in (B) and (C), III, the red shaded and white regions indicate light ON and OFF phases, respectively. Red and blue shaded regions in (B) and (C), II, denote SEM. (**D**) Bar chart with overlaid scatterplot of the CMi of diurnal cells (red bars), nocturnal cells (blue bars), and circadian independent cells (green bars) (*22*). The bar height and the whisker indicate the mean and maximum of CMi values, respectively. (**E**) Plots showing the evolution of CMi values for four representative cells (three diurnal cells and one nocturnal cell) that were recorded for three complete circadian cycles. Red and blue dashed lines in (D) and (E) indicate the threshold for defining diurnal and nocturnal cells, respectively. Three mice were used for circadian modulation study of RGC activity.

from five mice with chronic stability; additional examples are described below.

Fourth, to assess the range of RGC types we could detect, we stimulated the retinas in awake mice with a spatially varying grating designed to elicit responses from direction-selective (DS) and orientation-selective (OS) RGCs and investigated the capability to engage the same DS and OS RGCs chronically (*22*). The multiplexed measurements were made with the head rigidly restrained (Fig. 3, A and B, white arrow) to ensure a fixed visual field with respect to the moving grating displayed on a flat screen (movie S2) with alternating 2-s ON and OFF periods (Fig. 3C, pink and white vertical bars). Representative raster plot data from one of these channels on days 7 and 14 (Fig. 3C and fig. S6, B and C) highlight the chronically stable behavior of three spike-sorted RGCs, including spike waveforms, amplitudes, and raster plot responses. Specifically, average spike waveforms for these three neurons in the 10 trials each day, as well as between day 7 and day 14, exhibited minimal systematic change (fig. S9A), which was confirmed by auto- and cross-correlation analyses (fig. S9B). Moreover, polar plots of firing rate versus grating direction (Fig. 3C, middle) showed that these three neurons can be classified as follows: Neuron-1 (red) is a direction-selective ganglion cell (DSGC) with nasal-to-temporal (N→T) preference, neuron-2 (green) is a non-DSGC, and neuron-3 (blue) is a DSGC with ventral-to-dorsal (V→D) preference. The direction preference and selectivity remained stable from day 7 to day 14 after injection, and small variations between days were statistically insignificant (fig. S9, C and D). We note that the intact OKR driven by the moving gratings did not disrupt the chronic RGC recording stability (fig. S10), and that potential OKR-induced random variability was averaged from RGC responses over 10 consecutive trials of moving grating stimulation (*36*).

A summary of our in vivo 16-channel measurements from day 7 to day 14 (Fig. 3D and fig. S11) confirms the stable chronic recording across all channels. Overall, we recorded from 32 RGCs of which 15 were non-DSGCs, 3 were orientation-selective (OSGCs; 2 dorsal-ventral and 1 nasal-temporal), and 14 were DSGCs (2 D→V, 5 V→D, 3 N→T, and 4 T→N) (*22*). The direction selectivity indices (DSi's) and orientation selectivity indices (OSi's) (*22*) remained stable and no RGCs shifted categories between the two recording sessions (days 7 and 14), providing additional evidence that individual cells can be tracked for 2 weeks (Fig. 3E). Moreover, the percentages of DSGCs, OSGCs, and non-DSGCs (44%, 9%, and 47%, respectively) in this dataset are similar to those obtained from recent large-scale calcium imaging of >5000 RGCs in retinal explants (35%, 14.5%, and 51.5%; difference between the two datasets, $P > 0.05$ by χ^2 test) (*4*).

Finally, we asked whether we could use implanted mesh electronics to investigate circadian modulation of RGC activity (*22*). Specifically, we monitored RGCs at 4-hour intervals over several day/night cycles (Fig. 4A) for a total of 18 recordings (nocturnal, 8 p.m. to 8 a.m.; diurnal, 8 a.m. to 8 p.m.). Representative data from a DSGC in a mouse demonstrated that preferred direction and direction selectivity varied little during this period (fig. S12A). In contrast, the absolute firing rate in the preferred direction (±45°) varied in a consistent way over three complete circadian cycles (days 1 and 2, 4 and 5, and 6 and 7 after injection), with a firing rate during the diurnal phase that was on average 77% higher than during the nocturnal phase (Fig. 4B). Similar constancy of preferred direction but circadian variation of activity level was found for other RGCs, including a D→V DSGC and a non-DSGC (fig. S12, B and C).

Overall, of the 28 RGCs from three mice we recorded in this regime, 20 exhibited higher firing rates during the diurnal phase. Four others exhibited decreased firing rates during the diurnal phase, and the remaining four showed minimal circadian modulation, as assessed from their circadian modulation indices (CMi's; Fig. 4, C and D) (*22*). Cells that were tracked for three complete circadian cycles demonstrated that RGCs remained in the same circadian modulation categories, despite slight variations in CMi values (Fig. 4E). Interestingly, of six cells for which ON-OFF preferences were measured carefully, two of three diurnal-high cells were ON and one was ON-OFF, both of the nocturnal-high cells were OFF, and the sole invariant cell was ON-OFF, suggesting a correlation between RGC polarity and day/night modulation of activity that will be interesting to investigate. The pattern of increased diurnal firing activity for the majority of RGCs is consistent with results of a previous ERG study in which the b-wave amplitude, which reflects the population average of ON-bipolar cell activity (*37*), was found to increase in the daytime (*11*).

We have demonstrated multiplexed, chronically stable recording from diverse RGC types by means of syringe-injectable mesh electronics in mice. The ultraflexibility of mesh electronics allowed for nonsurgical intravitreal delivery into mouse eyes via noncoaxial injection and formation of conformal and chronically stable functional interface with the retina in vivo, which can be readily adapted for other animals with larger eyes. This method provides an attractive alternative to past studies of RGC activity in explants and offers important new insights into the dynamic information processing between the retina and other parts of the CNS.

REFERENCES AND NOTES

1. R. H. Masland, *Neuron* **76**, 266–280 (2012).
2. M. Hoon, H. Okawa, L. Della Santina, R. O. Wong, *Prog. Retin. Eye Res.* **42**, 44–84 (2014).
3. J. R. Sanes, R. H. Masland, *Annu. Rev. Neurosci.* **38**, 221–246 (2015).
4. T. Baden *et al*., *Nature* **529**, 345–350 (2016).
5. C. M. Lewis, C. A. Bosman, P. Fries, *Curr. Opin. Neurobiol.* **32**, 68–77 (2015).
6. E. J. Hamel, B. F. Grewe, J. G. Parker, M. J. Schnitzer, *Neuron* **86**, 140–159 (2015).
7. I. J. Kim, Y. Zhang, M. Yamagata, M. Meister, J. R. Sanes, *Nature* **452**, 478–482 (2008).
8. G. D. Field *et al*., *Nature* **467**, 673–677 (2010).
9. T. A. LeGates, D. C. Fernandez, S. Hattar, *Nat. Rev. Neurosci.* **15**, 443–454 (2014).
10. K. S. Korshunov, L. J. Blakemore, P. Q. Trombley, *Front. Cell. Neurosci.* **11**, 91 (2017).
11. C. R. Jackson *et al*., *J. Neurosci.* **32**, 9359–9368 (2012).
12. C. K. Hwang *et al*., *J. Neurosci.* **33**, 14989–14997 (2013).
13. B. H. Liu, A. D. Huberman, M. Scanziani, *Nature* **538**, 383–387 (2016).
14. D. E. Wilson, D. E. Whitney, B. Scholl, D. Fitzpatrick, *Nat. Neurosci.* **19**, 1003–1009 (2016).
15. O. S. Dhande, A. D. Huberman, *Curr. Opin. Neurobiol.* **24**, 133–142 (2014).
16. S. W. Kuffler, *J. Neurophysiol.* **16**, 37–68 (1953).
17. H. B. Barlow, R. M. Hill, W. R. Levick, *J. Physiol.* **173**, 377–407 (1964).
18. T.-M. Fu *et al*., *Nat. Methods* **13**, 875–882 (2016).
19. J. Liu *et al*., *Nat. Nanotechnol.* **10**, 629–636 (2015).
20. G. Hong *et al*., *Nano Lett.* **15**, 6979–6984 (2015).
21. T. Zhou *et al*., *Proc. Natl. Acad. Sci. U.S.A.* **114**, 5894–5899 (2017).
22. See supplementary materials.
23. J. J. Jun *et al*., *Nature* **551**, 232–236 (2017).
24. C. S. Nickerson, H. L. Karageozian, J. Park, J. A. Kornfield, *Invest. Ophthalmol. Vis. Sci.* **45**, 37 (2004).
25. X. Duan *et al*., *Neuron* **85**, 1244–1256 (2015).
26. I. J. Kim, Y. Zhang, M. Meister, J. R. Sanes, *J. Neurosci.* **30**, 1452–1462 (2010).
27. Y. Zhang, I. J. Kim, J. R. Sanes, M. Meister, *Proc. Natl. Acad. Sci. U.S.A.* **109**, E2391–E2398 (2012).
28. N. Suematsu *et al*., *Front. Syst. Neurosci.* **7**, 103 (2013).
29. D. Zoccolan, B. J. Graham, D. D. Cox, *Front. Neurosci.* **4**, 193 (2010).
30. K. Yonehara *et al*., *Neuron* **89**, 177–193 (2016).
31. G. T. Prusky, N. M. Alam, S. Beekman, R. M. Douglas, *Invest. Ophthalmol. Vis. Sci.* **45**, 4611–4616 (2004).
32. G. H. Jacobs *et al*., *Science* **315**, 1723–1725 (2007).
33. R. Q. Quiroga, Z. Nadasdy, Y. Ben-Shaul, *Neural Comput.* **16**, 1661–1687 (2004).
34. N. Schmitzer-Torbert, A. D. Redish, *J. Neurophysiol.* **91**, 2259–2272 (2004).
35. A. Jackson, E. E. Fetz, *J. Neurophysiol.* **98**, 3109–3118 (2007).
36. W. Sun *et al*., *Nat. Neurosci.* **19**, 308–315 (2016).
37. L. Gurevich, M. M. Slaughter, *Vision Res.* **33**, 2431–2435 (1993).

ACKNOWLEDGMENTS

We thank J. E. Dowling for helpful discussions, M. Meister for useful suggestions, and J. Huang for help with recording instrumentation. **Funding:** Supported by Air Force Office of Scientific Research grant FA9550-14-1-0136, Harvard University Physical Sciences and Engineering Accelerator award, and a NIH Director's Pioneer Award 1DP1EB025835-01 (C.M.L.); American Heart Association Postdoctoral Fellowship 16POST27250219 and NIH Pathway to Independence Award from NIA 1K99AG056636-01 (G.H.); a NIH R37 grant from NINDS NS029169 (M.Q. and J.R.S.); and the Harvard University Center for Nanoscale Systems supported by NSF. **Author contributions:** G.H., T.-M.F., M.Q., J.R.S., and C.M.L. designed the experiments; G.H., T.-M.F., M.Q., R.D.V., X.Y., T.Z., J.M.L., and H.-G.P. performed the experiments; G.H., T.-M.F., M.Q., J.R.S., and C.M.L. analyzed the data and wrote the paper; and all authors discussed the results and commented on the manuscript. **Competing interests:** None. **Data and materials availability:** All data are available in the manuscript or the supplementary materials. Mesh electronics probes are available upon request to the authors.

SUPPLEMENTARY MATERIALS

www.sciencemag.org/content/360/6396/1447/suppl/DC1
Materials and Methods
Figs. S1 to S12
Tables S1 and S2
Movies S1 and S2
References (*38*–*44*)

4 January 2018; accepted 26 April 2018
10.1126/science.aas9160

A method for single-neuron chronic recording from the retina in awake mice

Guosong Hong, Tian-Ming Fu, Mu Qiao, Robert D. Viveros, Xiao Yang, Tao Zhou, Jung Min Lee, Hong-Gyu Park, Joshua R. Sanes and Charles M. Lieber

Science **360** (6396), 1447-1451.
DOI: 10.1126/science.aas9160

Eye can see neural activity

Organisms take up a tremendous amount of information through the visual system, which is then processed by the neural circuitry. Hong *et al.* developed a mesh electronics implant that is delivered by injection into mice retinas. With these devices, it is possible to obtain recordings from retinal ganglion cells over long time periods in awake, active mice. Both orientation- and direction-selective retinal ganglion cells can be monitored, as can the circadian modulation of retinal ganglion cell activity.

Science, this issue p. 1447

Supplementary Materials for

A method for single-neuron chronic recording from the retina in awake mice

Guosong Hong, Tian-Ming Fu, Mu Qiao, Robert D. Viveros, Xiao Yang, Tao Zhou, Jung Min Lee, Hong-Gyu Park, Joshua R. Sanes, Charles M. Lieber*

*Corresponding author. Email: cml@cmliris.harvard.edu

Published 29 June 2018, *Science* **360**, 1447 (2018)
DOI: 10.1126/science.aas9160

This PDF file includes:

Other supplementary material for this manuscript includes the following:

Movies S1 and S2

Materials and Methods

Design and fabrication of mesh electronics.

The syringe-injectable mesh electronics for non-surgical intravitreal delivery via non-coaxial injection and RGC electrophysiology from awake mouse retinas were fabricated according to geometrical design and fabrication procedure similar to our previous reports (*18-21*). Key parameters involved in the geometrical design of the mesh electronics are given as follows: (*i*) total mesh width, W=1.5 mm; (*ii*) longitudinal SU-8 ribbon width, w_1=10 μm, transverse SU-8 ribbon width, w_2=10 μm; (*iii*) angle between longitudinal and transverse SU-8 ribbons, α=70°; (*iv*) longitudinal spacing (pitch between transverse ribbons), L_1=333 μm, transverse spacing (pitch between longitudinal ribbons), L_2=100 μm; (*v*) metal interconnect line width, w_m=5 μm, total number of recording channels, N=16; (*vi*) longitudinal ribbons have three-layer sandwich structure (SU-8 polymer / metal / SU-8 polymer) and transverse ribbons have two-layer structure (SU-8 polymer / SU-8 polymer). Key steps involved in the fabrication procedure are described as follows: (*i*) A 3" Si wafer (n-type 0.005 Ω·cm, 600-nm thermal oxide, Nova Electronic Materials, Flower Mound, TX) was pre-cleaned with oxygen plasma (100 W, 5 min), and a sacrificial layer of Ni with a thickness of 100 nm was thermally evaporated (Sharon Vacuum, Brockton, MA) onto the Si wafer. (*ii*) Negative photoresist SU-8 (SU-8 2000.5; MicroChem Corp., Newton, MA) with a thickness of ca. 420 nm was spin-coated onto the Ni-coated Si wafer, pre-baked sequentially at 65 °C for 1 min and 95 °C for 4 min, and then patterned by photolithography (PL) with a mask aligner (ABM mask aligner, San Jose, CA). After photolithographically patterned UV light exposure the Si wafer was post-baked sequentially at 65 °C for 3 min and 95 °C for 3 min. (*iii*) After post-baking, the SU-8 photoresist was developed in SU-8 Developer (MicroChem Corp., Newton, MA) for 2 min, rinsed with isopropanol, dried

in a N_2 flow and hard-baked at 180 °C for 1 h. (*iv*) The wafer was then cleaned with oxygen plasma (50 W, 1 min), spin-coated with MCC Primer 80/20 and LOR 3A lift-off resist (MicroChem Corp., Newton, MA) sequentially, baked at 185 °C for 5 min, followed by spin-coating Shipley 1805 positive photoresist (Microposit, The Dow Chemical Company, Marlborough, MA), which was then baked at 115 °C for 5 min. The positive photoresist was patterned by PL to define the features of metal interconnect lines and developed in MF-CD-26 (Microposit, The Dow Chemical Company, Marlborough, MA) for 90 s. (*v*) A 1.5-nm thick Cr layer and a 100-nm thick Au layer were sequentially deposited by electron-beam evaporation (Denton Vacuum, Moorestown, NJ), followed by a lift-off step (Remover PG, MicroChem Corp., Newton, MA) to make the Au interconnect lines. (*vi*) Steps *iv* and *v* were repeated for PL patterning and deposition of the Pt recording electrodes (Cr: 1.5 nm, Pt: 50 nm). The diameter of Pt recording electrodes was 20 μm. (*vii*) Steps *ii* and *iii* were repeated for PL patterning of a top layer of the SU-8 polymer, which encapsulated and insulated the metal interconnect lines except for the exposed Pt recording electrodes. After hard-baking of top SU-8 layer at 180 °C for 1 h, the Si wafer with fabricated mesh electronics was hard-baked again at 190-195 °C to melt both top and bottom layers of SU-8 polymer and improve the fusion of both layers into a monolithic component. (*viii*) Finally, the Si wafer was transferred to a Ni etchant solution comprising 40% $FeCl_3$:39% HCl:H_2O=1:1:20 to remove the sacrificial Ni layer and release the mesh electronics from the Si substrate. Released mesh electronics were rinsed with sterile deionized (DI) water, transferred to a sterile aqueous solution of poly-D-lysine (PDL, 1.0 mg/ml, MW 70,000-150,000, Sigma-Aldrich Corp., St. Louis, MO) for 24 h for surface modification of amine functional groups to improve adhesion with the inner limiting membrane of the retina, and then transferred to a sterile 1X phosphate buffered saline (PBS) solution (HyClone™ Phosphate Buffered Saline,

Thermo Fisher Scientific Inc., Pittsburgh, PA) before use. Future work exploiting reported strategies to increase substantially the number of recording electrodes (*38*) and implementing appropriate topological designs to enable full coverage of the retinal cup, could enable larger-scale functional connectivity of the retina neural circuitry to be mapped in awake mice. Additionally, functional modification of the mesh surface to increase adhesion to the retina could extend long-term stability to the months to year scale demonstrated by mesh electronics implanted in the brain (*18, 21*), and decreases in the width of Au metal interconnects could further increase the optical transmittance of the mesh electronics probes above the 95% reported here.

Optical transmission spectroscopy of mesh electronics.

UV-Vis-NIR transmission spectrum of unfolded mesh electronics on a quartz slide was measured using a Cary Series UV-Vis-NIR spectrophotometer (Agilent Technologies, Santa Clara, CA), background-corrected for contribution from the quartz slide. The measured range was 300-1000 nm but only the spectrum in the range of 400-600 nm, which is visible to the mouse eye, is shown.

Vertebrate animals.

Adult (20-30 g) female CD-1 mice (6-8 weeks old, Charles River Laboratories, Wilmington, MA) were the vertebrate animal subjects used for chronic in vivo through-lens imaging and multiplexed RGC electrophysiology in this study. Exclusion criteria were pre-established: animals with failed injections (e.g., severe bleeding, cataract development, or clouding of

vitreous body) or substantial acute damage to the eye (>20 μL of initial liquid injection volume) were discarded from further chronic recordings.

TYW3 transgenic mice (4-6 weeks old) were used for acute ex vivo confocal imaging of the interface between injected mesh electronics and RGCs. This mouse line was characterized in previous publications (*25, 26*). Several types of RGCs are labeled by yellow fluorescent protein (YFP) in the TYW3 mouse line.

Randomization or blinding study was not applicable to this study. All procedures performed on the mice were approved by the Animal Care and Use Committee of Harvard University. The animal care and use programs at Harvard University meet the requirements of the Federal Law (89-544 and 91-579) and NIH regulations and are also accredited by the American Association for Accreditation of Laboratory Animal Care (AAALAC). Animals were group-housed on a 12 h: 12 h light: dark cycle in the Harvard University's Biology Research Infrastructure (BRI) and fed with food and water *ad libitum* as appropriate.

Non-surgical delivery of mesh electronics into live mouse eyes.

Non-coaxial injection of mesh electronics onto the mouse retina. In vivo non-surgical intravitreal injection of mesh electronics into the eyes of live mice was performed using a controlled non-coaxial injection method. First, all metal and glass tools in direct contact with the subject were autoclaved for 1 h before use, and all plastic tools in direct contact with the subjects were sterilized with 70% ethanol and rinsed with sterile DI water and sterile 1X PBS before use. Prior to injection, the mesh electronics were sterilized with 70% ethanol followed by rinsing in sterile DI water and transfer to sterile 1X PBS. Mesh electronics probe was then loaded into a sterile borosilicate capillary tube with an inner diameter (ID) of 200 μm and an outer diameter (OD) of

330 μm (Produstrial LLC, Fredon, NJ) using the standard procedure described in previous publications (*18, 20*). The use of a needle with smaller diameter (OD = 330 μm, similar to a 29-gauge hypodermic needle) than previously reported (OD = 650 μm) for brain injection (*18, 20, 21*) is critical to ensure success of injection without causing significant damage and bleeding to the mouse eye.

CD-1 mice were anesthetized by intraperitoneal injection of a mixture of 75 mg/kg of ketamine (Patterson Veterinary Supply Inc., Chicago, IL) and 1 mg/kg dexdomitor (Orion Corporation, Espoo, Finland). The degree of anesthesia was verified via the toe pinch method before the operation started. To maintain the body temperature and prevent hypothermia of the subject, a homeothermic blanket (Harvard Apparatus, Holliston, MA) was set to 37 °C and placed underneath the anesthetized mouse. GenTeal lubricant eye gel (Alcon, Fort Worth, TX) was applied on both eyes of the mouse to moisturize the eye surface throughout the operation.

For intracortical implantation of the grounding screw for chronic electrophysiological recording from the retina, the mouse was placed in prone position and fixed with the stereotaxic frame. Hair removal lotion (Nair®, Church & Dwight, Ewing, NJ) was applied to the scalp for depilation of the mouse head and iodophor was applied subsequently to sterilize the depilated scalp skin. A 1-mm longitudinal incision along the sagittal sinus was made in the scalp with a sterile scalpel, and the scalp skin was resected using surgical scissors to expose a 6 mm × 8 mm (mediolateral × anteroposterior) portion of the skull. METABOND® enamel etchant gel (Parkell Inc., Edgewood, NY) was applied over the exposed cranial bone to prepare the surface for mounting the grounding screw and interface cable on the mouse skull later. A 1 mm diameter burr hole was drilled using a dental drill (Micromotor with On/Off Pedal 110/220, Grobet USA, Carlstadt, NJ) according to the following stereotaxic coordinates: anteroposterior: -4.96 mm,

mediolateral: 3.10 mm (in the left hemisphere). After the hole was drilled, the dura was carefully incised and resected using a 27-gauge needle (PrecisionGlide®, Becton Dickinson and Company, Franklin Lakes, NJ). Then a sterilized 0-80 set screw (18-8 Stainless Steel Cup Point Set Screw; outer diameter: 0.060" or 1.52 mm, groove diameter: 0.045" or 1.14 mm, length: 3/16" or 4.76 mm; McMaster-Carr Supply Company, Elmhurst, IL) was screwed into this 1-mm burr hole to a depth of 500 μm as the grounding and reference electrode. METABOND® dental cement (Parkell Inc., Edgewood, NY) was used to fix the junction between the implanted grounding screw and the skull.

For non-coaxial intravitreal injection of mesh electronics into the mouse eye, the mouse was placed in right/left lateral decubitus position in the stereotaxic frame to expose its left/right eye for injection. The GenTeal lubricant eye gel previously applied the eyes was gently removed only at the lateral and medial canthi of the eye with sterile surgical spears (Braintree Scientific Inc., Braintree, MA), and the exposed area was swabbed with 70% ethanol and sterile 1X PBS. A sterile 27-gauge needle was used to puncture a hole for sclerotomy ca. 1 mm below the limbus at the lateral canthus (*39*) for subsequent non-coaxial injection of mesh electronics and another hole at the medial canthus for draining the injected liquid to reduce intraocular pressure during injection. The 200 μm ID and 330 μm OD capillary needle loaded with mesh electronics was mounted onto the stereotaxic stage (fig. S1, A and B) through a micropipette holder (Q series holder, Harvard Apparatus, Holliston, MA), which was connected to a 5 mL syringe (Becton Dickinson and Company, Franklin Lakes, NJ) through a polyethylene Intramedic™ catheter tubing (I.D. 1.19 mm, O.D. 1.70 mm). The sterilized capillary needle was allowed to advance through the pre-punctured hole at the lateral canthus of the eye until its tip reaches the nasal part of the retina, taking special caution to avoid damaging the lens (fig. S2, A and B). The mesh

electronics was injected into the eye using a non-coaxial injection method (Fig. 1A, III, fig. S1C and fig. S3) adapted from our previously reported controlled injection approach (*18, 20*). Notably, the non-coaxial injection setup was built upon conventional stereotaxic frame used for brain probe implantation and is readily adaptable by other labs. In brief, controlled non-coaxial injection was achieved by balancing the volumetric flow rate (typically 3-7 mL/h), which was controlled by a syringe pump (PHD 2000, Harvard Apparatus, Holliston, MA), and the near-horizontal needle withdrawal speed (typically 0.2-0.5 mm/s), which was controlled by a motorized linear translation stage (860A motorizer and 460A linear stage, Newport Corporation, Irvine, CA). During the controlled non-coaxial injection process, an eyepiece camera (DCC1240C, Thorlabs Inc., Newton, NJ) was used to ensure field of view (FoV) visualization of the trajectory of the top end of mesh electronics that followed a pre-defined trajectory computed numerically in MATLAB based on the radius of curvature of the mouse eye, allowing conformal placement of the bottom end of the mesh electronics on the concave retina surface during injection (Fig. 1A, III, fig. S1C and fig. S3). After 2-3 mm length of mesh electronics was injected non-coaxially, conventional coaxial injection was employed simultaneously with needle withdrawal, expelling the external portion of mesh electronics with recording electrodes while allowing the capillary needle to exit the insertion hole at the lateral canthus (fig. S2, C and D). For successful long-term single-neuron recording from the retina in awake mice, the total injection volume is usually between 5 and 20 μL. An unexpected large injection volume (>20 μL) could result in significant clouding of vitreous body that does not improve over time or bleeding from the corneal vessels, leading to expulsion of the subject from the study. An ample amount of water was injected extraocularly to fully expel the remaining mesh electronics from the capillary needle (fig. S2D). The junction between the mesh electronics and the lateral canthus

of the eye was protected with a small amount of Kwik-Sil adhesive silicone elastomer (World Precision Instruments Inc., Sarasota, FL) to be later covered with dental cement (see below) while the draining hole at the medial canthus of the eye was sealed with a small amount of 3M™ Vetbond™ Tissue Adhesive (Santa Cruz Biotechnology Inc., Dallas, TX). Antibiotic ointment (WATER-JEL Technologies LLC) was applied copiously on the eye after injection.

Electrical connection of mesh electronics for chronic recording. After non-coaxial intravitreal injection of mesh electronics into the mouse eye, the fully expelled mesh electronics was unfolded onto a 16-channel flexible flat cable (FFC, PREMO-FLEX, Molex Incorporated, Lisle, IL) to expose the I/O connection pads. High-yield bonding of mesh electronics I/O pads to the FFC was carried out using our reported conductive ink printing method (*18*, *20*). In brief, the print head loaded with carbon nanotube solution (Stock No.: P093099-11, Tubes@Rice, Houston, TX) was driven by a motorized micromanipulator (MP-285/M, Sutter Instrument, Novato, CA) through a user-written LabVIEW program to print conductive ink automatically and connect each mesh I/O pad to a corresponding contact electrode in the FFC to enable independently addressable recording elements. Failure of mesh I/O unfolding could lead to potential low-yield electrical connection to the FFC interface cable. All printed conductive lines were passivated by METABOND® dental cement, and then the entire FFC with mesh electronics bonded to the FFC was cemented to the mouse skull with METABOND® dental cement. Additional dental cement was carefully applied to cover the silicone previously applied at the lateral canthus of the injected mouse eye for protection of mesh electronics without touching any part of the mouse eye, eyelids or the mesh, resulting in a monolithic piece of dental cement protecting the mesh electronics and the FFC, and a chronically stable interface for long-term retina electrophysiology. The FFC was folded to reduce its size on the mouse skull. A

mouse head-plate made of poly(lactic acid) (PLA), which comprises an opening in the middle to fit the FFC and the grounding screw and two untapped free-fit holes (hole diameter: 0.177" or 4.50 mm) in both wings for 8-32 screws, was made by a Makerbot 3D printer (MakerBot Industries, Brooklyn, NY) and also cemented to the skull using METABOND® dental cement for head-fixation during retina recording and pupil tracking.

Postoperative care. After operation was complete, additional antibiotic ointment was applied on the injected mouse eye, and GenTeal lubricant eye gel was applied on both eyes of the mouse to moisturize the eye surface, before the mouse was returned to the cage equipped with a 37°C heating pad and its activity monitored every hour until fully recovered from anesthesia (i.e., exhibiting sternal recumbency and purposeful movement). Buprenex (Buprenorphine, Patterson Veterinary Supply Inc, Chicago, IL) analgesia was given intraperitoneally at a dose of 0.05 mg/kg body weight every 12 h for up to 72 h post eye injection.

In vivo through-lens imaging of mouse retina.

In vivo through-lens imaging of the retina was performed on live mice before and after non-coaxial injection of mesh electronics to characterize the chronic interface between the injected mesh and the retina. We invented a ‘liquid Hruby lens’ by modifying the original design of the conventional Hruby lens (*40*) widely used in ophthalmic fundus photography with transparent eye lubricant gel to counteract the intrinsic focusing power of the lens in mouse eye. This ‘liquid Hruby lens’ allows for microscopic imaging of eye fundus directly through the lens in a live animal with a conventional wide-field microscope of any working distance.

To implement the ‘liquid Hruby lens’ for mouse eye fundus imaging, the mouse was anesthetized by intraperitoneal injection of a mixture of 75 mg/kg of ketamine and 1 mg/kg

dexdomitor, before 1-2 drops of 1 wt% atropine sulfate ophthalmic solution was applied to the eye of interest. The ophthalmic solution was allowed to cover the surface of the eye for ca. 5 min to afford complete dilation of the pupil before the eye was rinsed with 1X PBS. GenTeal lubricant eye gel (Alcon, Fort Worth, TX) was used to cover the dilated eye and a micro cover glass (25 mm × 25 mm, VWR International, Radnor, PA) was gently placed on the applied eye lubricant to flatten the gel/air interface. A 'liquid Hruby lens' was thus formed between the curved surface of the cornea and the flat cover slip with matching but opposite focusing power to the cornea and lens owing to similar refractive index of the lubricant gel to those of cornea and lens. A home-built white-light and wide-field microscope (fig. S4, A and B) was used to take eye fundus images at different magnifications in two different modes: in the bright-field (normal illumination) mode, the optical axis of observation is within a range of 5º from that of illumination to afford the maximum contrast of retinal blood vasculature while the mesh electronics appears to have low contrast due to large porosity of mesh design and minimum blockage of illuminating/reflected light; in the pseudo-dark-field (oblique illumination) mode, the optical axis of observation is 30-40º from that of illumination to afford collection of scattered light off the longitudinal Au interconnect lines and Pt recording electrodes and improve the contrast for imaging the mesh electronics inside the mouse eye. Different magnifications of in vivo eye fundus imaging were afforded by selecting microscopic objectives with different magnification powers. Due to strong scattering of photons by Au and Pt, the interconnects and recording electrodes generally appeared larger than their actual sizes. After imaging, the cover slip was removed and additional eye lubricant gel was applied copiously on both eyes, and the mouse was returned to the cage equipped with a 37°C heating pad and its activity monitored every hour until fully recovered from anesthesia.

Ex vivo imaging of the mesh-retina interface.

For ex vivo confocal imaging based on the intrinsically expressed YFP fluorescence in certain RGCs, transgenic mouse line TYW3 (*25, 26*) was injected with mesh electronics in the eye using aforementioned non-coaxial injection approach, and the degree of unfolding and area of coverage of mesh electronics on the retina were examined with the in vivo through-lens eye fundus camera to ensure successful non-coaxial injection and conformal coating of the mesh electronics onto the retina surface. Mesh electronics used for ex vivo imaging had SU-8 polymer doped with Rhodamine B to afford fluorescence labeling of the mesh ribbons. Mice with good injections of mesh electronics in the eye were sacrificed by intraperitoneal injection of Euthasol at a dose of 270 mg/kg body weight, and injected eyes were carefully resected and fixed in fresh 4% paraformaldehyde in 1X PBS at 4 ºC for 1 h without disturbing the mesh electronics in the vitreous humor. After fixation, the lens was carefully removed with spring scissors (15009-08, Fine Science Tools, Foster City, CA) to allow 3D confocal scanning of the mesh-retina interface without distortion of wavefront due to curvature of the lens. Retina whole mount images were obtained on an LSM 880 microscope at 10X (Zeiss, Jena, Germany) in the YFP channel using an excitation of 488 nm to collect the YFP fluorescence from endogenously labeled RGCs, and an excitation of 561 nm to collect the Rhodamine B fluorescence from the SU-8 polymer component of mesh ribbons. All confocal images were taken using a 1-AU pinhole. For acquisition of low-resolution confocal images, a voxel size of 3 μm × 3 μm × 5.8 μm ($x \times y \times z$) was used in a Tile Scan mode, resulting in a 3×3 composite image with a total volume of 3.6 mm × 3.6 mm × 1.1 mm (1200 × 1200 × 200 voxels). For acquisition of high-resolution confocal images, a voxel size of 1.2 μm × 1.2 μm × 1 μm ($x \times y \times z$) was used to scan a single tile,

resulting in a volume of 1.2 mm × 1.2 mm × 0.5 mm (1024 × 1024 × 500 voxels). Note that the dark shadow for some mesh ribbons in the high-resolution image in Fig. 1C, II, which appears only at the proximal side of the optic disk, is due to a small degree of excitation/fluorescence light attenuation by mesh ribbons and has nothing to do with the normal distribution of RGCs. 3D reconstruction of confocal images was performed using ImageJ software with false red color for fluorescence signals of Rhodamine B and false green color for fluorescence signals of YFP. 3D reconstructed images were used to analyze the average distance between an electrode and the closest labeled RGCs, while the distance between an electrode and the closest RGC (labeled or unlabeled) should be even smaller given that only 10% of RGCs were labeled with YFP in the TYW3 mouse line.

In vivo eye imaging and pupil tracking.

CD-1 mouse injected with mesh electronics into its eye on different days post-injection or age-matched control CD-1 mouse without any injection of mesh electronics into either eye was restrained in a Tailveiner® restrainer (Braintree Scientific LLC., Braintree, MA). The same head-plate was cemented to the exposed skull of the control mouse in a similar manner as described above in "*Non-surgical delivery of mesh electronics into live mouse eyes*". The skull-cemented head-plate was fixed to two Ø1/2" optical posts (Thorlabs Inc., Newton, NJ) through the two untapped free-fit holes in both wings with two 8-32 screws. The two optical posts were mounted to a frame assembled from standard optomechanical components prefixed on an optical breadboard (Thorlabs Inc., Newton, NJ). A near-infrared (NIR) light-emitting diode (LED) (emission wavelength: 850 nm, power: 35 mW, M850L2, Thorlabs Inc., Newton, NJ) invisible to the mouse eye was used for illumination of the eye of interest, while a Watec CCD camera

operating in the NIR range (WAT-502A, Newburgh, NY) was used for collecting dynamic video-rate (25 frames per second) NIR images of the mouse eye during blink reflex, pupillary reflex, optokinetic reflex (OKR) and visual acuity tests with details as follows:

1) For imaging the blink reflex, a gentle air puff was given to the eye of interest every 15 s while the Watec CCD camera captured the NIR eye images continuously.

2) For imaging the pupillary reflex, the white light power density impinging on the pupil was modulated between 23.95 $\mu W/cm^2$ for the 'light ON' phase with 15-s duration and 0.24 $\mu W/cm^2$ for the 'light OFF' phase with 15-s duration while the Watec CCD camera captured the NIR pupil images continuously. Light intensity was measured with a silicon photodetector (918D-UV-OD3, Newport Corporation, Irvine, CA).

3) For evoking and imaging the OKR, a computer screen (20.5"×12.5") was placed a distance of 20 cm from both eyes of the mouse, covering an azimuth angle range of ±52°, similar to previously reported protocols (*29*). Given an average mouse eye diameter of 3 mm, this resulted in a lateral magnification of 0.015 (meaning the image was demagnified) for images of the computer screen formed on the mouse retina. Gratings comprising alternating white and black bars filling the entire screen and moving in two opposite horizontal directions (east→west and west→east) were programmed in MATLAB. The east-west horizon was defined as the line connecting the medial and lateral canthi of the eye of interest. The grating moved in each direction for 10 s at a constant speed of 34 mm/s, equivalent to 0.51 mm/s for images on the retina, or an angular velocity of 9.74°/s with small-angle approximation. This angular velocity is within the reported optimum grating speed range of 6.28-31.4°/s to evoke OKR in mice (*13*). The pitch of grating was fixed at 32 mm/cycle on the computer screen, equivalent to 0.48 mm/cycle on the retina or 0.11 cycles per degree (cpd). The average power density of moving

grating on the computer monitor was 10.1 μW/cm^2. One complete OKR episode is defined as a slow phase of pupil positional drift followed by a fast phase for the pupil to return to its original position, and the OKR is quantified by analyzing the number of OKR episodes, or eye-tracking movements per minute (ETMs/min) (*30*).

4) For studying visual acuity, the OKR test was carried out with varying spatial frequency of the moving grating ranging from 8 to 32 mm/cycle on the screen, equivalent to 0.11-0.44 cpd, with the moving speed fixed at 0.51 mm/s or 9.74°/s. Visual acuity was defined as the smallest grating pitch that was able to evoke OKR.

Mice used for all aforementioned reflex studies were injected with mesh electronics in both eyes to rule out the possibility of observed reflex driven by the intact eye, while the control animals were age-matched mice with no injection in either eye.

In vivo chronic retina electrophysiology in mice.

Mice with mesh electronics injected into the eye were recorded chronically on a daily basis, starting from Day 0 post-injection (i.e., ca. 5 h after injection on the same day injection was performed). Mice were restrained in a Tailveiner® restrainer (Braintree Scientific LLC., Braintree, MA) with the head-plate secured to reduce mechanical noise during recording and fix the visual field of the recorded eye during visual stimulation. Head-mounted FFC was connected to an Intan RHD 2132 amplifier evaluation system (Intan Technologies LLC., Los Angeles, CA) through a home-made printed circuit board (PCB). The 0-80 set screw was used as a reference. Electrophysiological recording was made when different visual stimuli were given to the mouse eye, including:

1) Light ON and OFF cycles: flash light with power density impinging on the pupil modulated between 23.95 μW/cm^2 for the 'ON' phase with 2-s duration and 0.24 μW/cm^2 for the 'OFF' phase with 2-s duration was used for identification of RGCs with different polarities (ON- and OFF-center RGCs). The spot size of the flash light was estimated as ~100 μm on the retina. We have tracked the same ON/OFF cells for a total of 11 times over 14 days based on chronic single-unit recordings.

2) Moving gratings: gratings comprising alternating white and black bars filling the entire computer screen (20.5"×12.5") and moving in different directions were programmed in MATLAB. A complete moving grating test comprised 10 repetitive trials, where each trial comprised eight different directions (east, northeast, north, northwest, west, southwest, south and southeast) in a randomized sequence. The mouse eye was light adapted by exposing it to the same moving grating without recording for 1 min before recording started. The grating moved in each direction for 2 s, with a 2-s interval of black screen between two directions, resulting in 32 s for a complete trial comprising a randomized sequence of eight moving directions. All directions are with respect to the horizon (east-west), which was defined as the line connecting the medial and lateral canthi of the eye of interest. When moving grating was displayed on the computer monitor, it had an average power density of 10.1 μW/cm^2, in comparison to an average power density of 1.7 μW/cm^2 when black screen was shown. The computer display was placed at a distance of 20 cm from the mouse eye, resulting in a lateral magnification of 0.015 (which means the image was demagnified on the retina) given the mouse eye diameter of 3 mm. Each bar had a width of 5.4 mm on the computer screen, corresponding to a width of 81 μm on the retina based on the lateral magnification of 0.015. Grating moved at a speed range of 22.7~56.7 mm/s in all directions on the computer screen, corresponding to a moving speed range of 0.34~0.85 mm/s

(with an optimum speed of 0.51 mm/s to evoke maximum response from DSGCs) on the mouse retina given the same lateral magnification.

Electrophysiological recording was synchronized with light intensity modulation and moving grating stimulation for analysis of different subtypes of RGCs. Data were acquired with a 20-kHz sampling rate and a 60-Hz notch filter, while the electrical impedance at 1 kHz of each recording electrode was also measured by the same Intan system.

3) Circadian modulation: mice injected with mesh electronics in the eye were housed on a 12 h: 12 h light: dark cycle before and during the study of circadian modulation. The ambient light has a power density of 81 $\mu W/cm^2$ during the diurnal phase (8 am – 8 pm) and 0.05 $\mu W/cm^2$ during the nocturnal phase (8 pm – 8 am). For study of circadian modulation, mice were recorded for single RGC responses to moving gratings as detailed above at six evenly spaced time points in a complete circadian cycle of 24 h, resulting in sampling times of 2:30 am, 6:30 am, 10:30 am, 2:30 pm, 6:30 pm and 10:30 pm with a margin of ± 90 min for each time point. For each time point, the moving grating stimulation protocol comprised 20 repetitive trials, where each trial comprised same eight different directions as above, after the mouse eye was light adapted for 1 min. The light stimulus power density on the mouse retina was estimated as 0.77 $\mu W/cm^2$, 0.58 $\mu W/cm^2$, 0.44 $\mu W/cm^2$ and 0.13 $\mu W/cm^2$ during the diurnal grating on, nocturnal grating on, diurnal grating off and nocturnal grating off periods, respectively, based on light intensity and pupil diameter measurements. Moving grating stimulation with simultaneous recording was performed at the same six time points on three different circadian cycles (Days 1-2, 4-5 and 6-7 post-injection) to demonstrate consistent recording from the same RGCs with reproducible results, resulting in a total of 18 times over 7 days for tracking the same single units chronically.

Data analysis of retina and pupil imaging and electrophysiological recording.

Data analysis of through-lens retina imaging. Since the in vivo through-lens retina imaging is a 2D projection of a 3D concave retina cup, any distance measurement requires calibration and correction based on local slope as follows. As demonstrated in fig. S4F, when an electrode and a landmark vessel are close (i.e. $d << R$), we can apply small-angle approximation and obtain:

$$d = \frac{d'}{\cos\alpha} \tag{1}$$

where d' is the projected distance (i.e., measured distance in through lens images) and cosα can be estimated by measured distance (d'_0) of two neighboring electrodes in the same row in the 2D projected image with known actual distance (d_0) in the proximal region. Together, the actual distance d between an electrode and its closest landmark can be estimated by:

$$d = \frac{d_0}{d'_0} \cdot d' \tag{2}$$

where d_0=292 μm based on the mesh design. Gaussian fitting is used to localize the center position of the electrode with a spatial resolution down to ~1 μm.

Data analysis of pupil imaging. Dynamic NIR imaging of pupil was analyzed by a user-written MATLAB software that recognizes the boundary of pupil based on contrast difference and fits the identified pupil boundary to a circle. Both the diameter and center location of the fitted circle were extracted for each frame of the NIR video of pupil tracking. The pupil diameter was plotted as a function of time with respect to timing of the light on/off cycles for pupillary reflex test, from which the pupil constriction was quantified by calculating the percentage reduction of pupil size from light OFF phase to ON phase (*41*). The pupil center location was plotted as a function of time with respect to moving gratings shown on the computer screen in different directions and with varying spatial frequencies for OKR and visual acuity tests.

Data analysis of electrophysiological recording. The electrophysiological recording data was analyzed offline in a similar manner to our previous report (*18*). In brief, raw recording data was filtered using non-causal Butterworth bandpass filters ('filtfilt' function in MATLAB) in the 250-6000 Hz frequency range to extract single-unit spikes of RGCs (*18, 42*). Single-unit spike sorting was performed by amplitude thresholding of the filtered traces and automatically determines the threshold based on the median of the background noise according to the improved noise estimation method (*33*). The signal-to-noise ratio (SNR) for each recording channel was calculated by dividing the average peak-to-peak amplitude of all sorted spikes by noise derived from noise estimation of a typical 1-min recording trace (fig. S7A). Sorted spikes were clustered to determine the number of single neurons and to assign spikes to each single neuron based on principal component analysis (PCA) using the WaveClus software that employs unsupervised superparamagnetic clustering of single-unit spikes (*33*). To assess the quality of cluster separation, the L-ratio for each cluster of spikes was calculated as follows (*43*),

$$L_{\text{ratio}} = \frac{L(C)}{N(C)} = \frac{\sum_{i \notin C} 1 - CDF_{\chi^2}(D^2_{i,C})}{N(C)} \tag{3}$$

where $N(C)$ denotes the total number of spikes in the cluster, CDF_{χ^2} represents the cumulative distribution function of the χ^2 distribution, and $D^2_{i,C}$ is the Mahalanobis distance of a spike i from the center of the cluster C. An L-ratio of < 0.05 is considered good cluster separation/isolation (*34*).

The autocorrelation and cross-correlation of average spike waveforms shown in figs. S8B, S9B and S10C were computed based on the standard Pearson product-moment correlation coefficient calculated as follows,

$$Corr(Y_1, Y_2) = \frac{\int_0^T \left(Y_1(t) - \overline{Y_1}\right)\left(Y_2(t) - \overline{Y_2}\right) dt}{\sqrt{\int_0^T \left(Y_1(t) - \overline{Y_1}\right)^2 \left(Y_2(t) - \overline{Y_2}\right)^2 dt}} \quad (4)$$

where $Y_1(t)$ and $Y_2(t)$ are two spike waveforms with a total duration T of 3 ms for each spike (*35*). The correlation histograms show the percentage distributions of correlation coefficients (i.e., waveform similarity) defined in Equation (4) for all pairwise comparisons between the average spike waveforms within the same group (autocorrelation) and between groups (cross-correlation). A value of 1 indicates identical spike shapes, irrespective of absolute spike amplitudes.

For each sorted and clustered spike, a firing time was assigned and all spike firing times belonging to the same cluster (i.e., the same neuron) were used to compute the firing rates in response to different visual stimuli for diverse RGC subtypes on different days post-injection. Analysis of single-unit firing events was different for the two different visual stimulation protocols:

1) Light ON and OFF cycles: Firing rate was computed by dividing the number of firing events of the same putative neuron over the time duration of each 'ON' or 'OFF' phase (Fig. 2E). Analysis of the variance (ANOVA) was performed using the built-in function 'anova1' in Matlab to evaluate the statistical significance between firing rates during light 'ON' and 'OFF' phases on the same day, and between different days during the same phase of light intensity modulation, for each identified neuron. The ON-OFF index (OOi) is defined as

$$OOi = \frac{\overline{r_{ON}} - \overline{r_{OFF}}}{\overline{r_{ON}} + \overline{r_{OFF}}} \quad (5)$$

where $\overline{r_{\mathrm{ON}}}$ and $\overline{r_{\mathrm{OFF}}}$ are defined as the average firing rates during the 'ON' and 'OFF' phases, respectively (*4*).

2) Moving gratings: Firing events of each putative neuron after spike sorting and clustering were plotted as short vertical ticks in a raster plot (Fig. 3C and fig. S6B) that is aligned to the onset of the moving grating stimulation protocol. The number of firing events for a specific moving direction of the grating was averaged over 10 trials, divided by the duration of each visual stimulus (2 s), and repeated for all eight directions, and the angular distribution of firing rates were plotted in the polar plots to reveal direction preference and selectivity of the recorded RGCs (Fig. 3C and fig. S11). The direction preference angle θ_{pref} is defined as follows by vector sum,

$$\theta_{pref} = \arg\left[\sum_{k=1}^{8} r_k \exp(i\theta_k)\right] \tag{6}$$

where r_k and θ_k are the average neuron firing rate and angle of the kth direction of moving gratings, respectively (*44*).

The direction selectivity index (DSi) is defined as

$$DSi = \frac{\overline{r_{pref}} - \overline{r_{opp}}}{\overline{r_{pref}} + \overline{r_{opp}}} \tag{7}$$

where $\overline{r_{\text{pref}}}$ and $\overline{r_{\text{opp}}}$ are defined as the average firing rates during moving grating of the preferred direction and that of the opposite direction, respectively. Similarly, the orientation selectivity index (OSi) is defined as

$$OSi = \frac{\overline{r_{pref}} - \overline{r_{ortho}}}{\overline{r_{pref}} + \overline{r_{ortho}}} \tag{8}$$

where $\overline{r_{\text{pref}}}$ and $\overline{r_{\text{ortho}}}$ are defined as the average firing rates during moving grating of the preferred orientation and that of the orthogonal orientation to the preferred orientation, respectively. A DSi or OSi of greater than 0.3 is used to assign a specific single unit to DSGC or

OSGC, respectively, with a DSi or OSi smaller than 0.3 assigned to a non-DSGC (*44*). Cross-correlation analysis of spikes trains assigned to neurons belonging to different channels but showing similar direction selectivity was carried out to identify potential overlap of recording across channels, that is, the same RGC recorded by more than one electrodes, which was removed from the total count of RGCs in Fig. 3D.

3) Circadian modulation: Angular distribution of firing rates was analyzed and plotted in the polar plots in the same way as aforementioned, and the firing rates during gratings moving in the preferred direction ± 45° (three directions in total) were averaged and used as the characteristic firing rate for a specific circadian time at which the recordings were acquired. Firing rates at six circadian times were averaged over three complete circadian cycles to demonstrate reproducibility of the observed circadian modulation of RGC activity. The circadian modulation index (CMi) is defined as

$$CMi = \frac{\overline{r_{day}} - \overline{r_{night}}}{\overline{r_{day}} + \overline{r_{night}}} \tag{9}$$

where $\overline{r_{\mathrm{day}}}$ and $\overline{r_{\mathrm{night}}}$ are defined as the average firing rates at the three diurnal times (10:30 am, 2:30 pm, 6:30 pm) and that at the three nocturnal times (10:30 pm, 2:30 am and 6:30 am), respectively. A CMi of greater than 0.1 is used to assign a specific single unit as a diurnal cell, a CMi of smaller than -0.1 assigned as a nocturnal cell, and a CMi between -0.1 and 0.1 as a circadian independent cell.

Statistical analysis.

For all statistical analyses, Matlab, Origin, and Excel were used. All replicate numbers, error bars, P values and statistical tests are indicated in the figures legends. For experiments where

statistical significance is demonstrated, sample sizes were selected to achieve at least 80% power at an alpha level of 0.05.

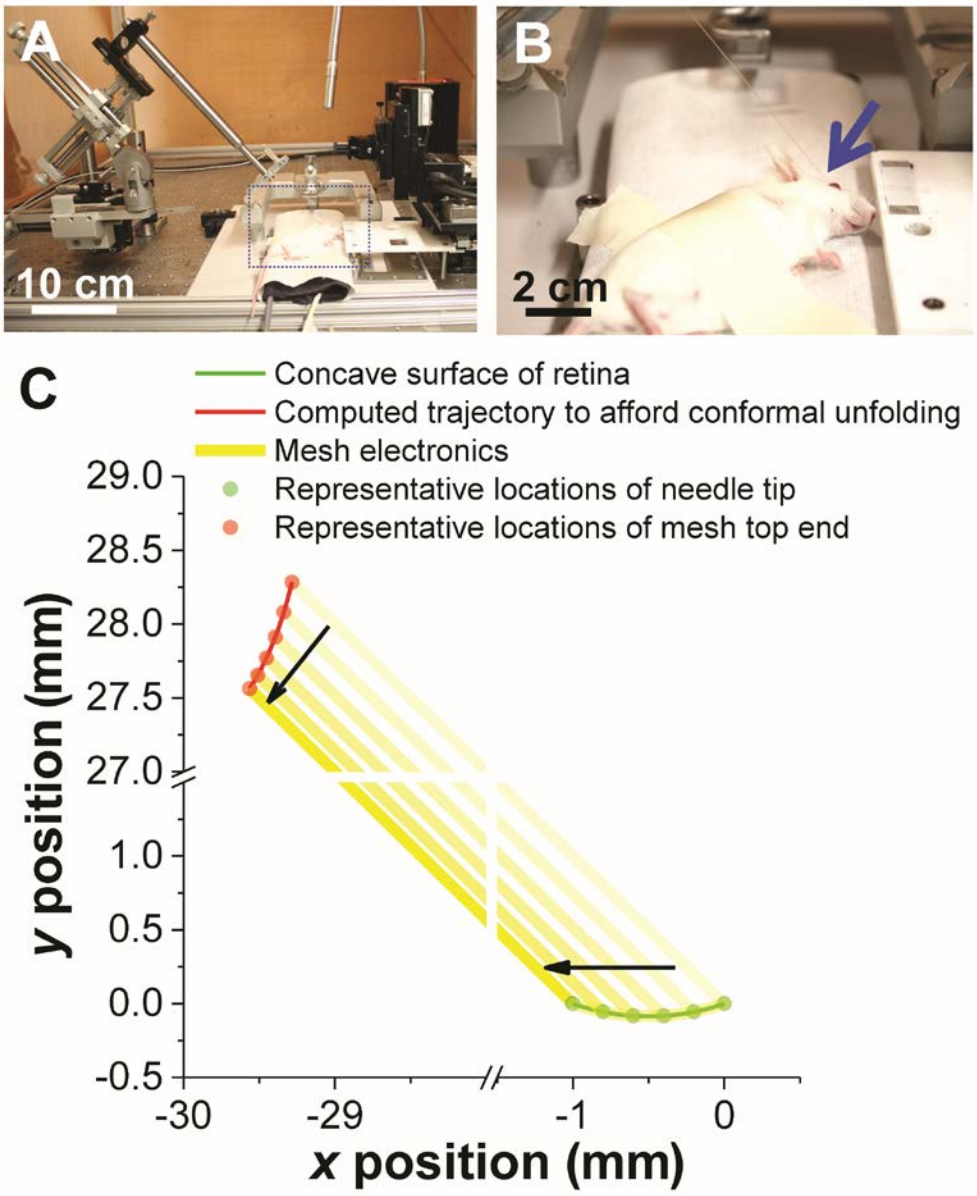

Fig. S1. Non-coaxial injection of mesh electronics for conformal positioning onto the retina surface. (**A** and **B**) Bright-field images of the in vivo non-surgical injection apparatus (**A**, with the blue dashed box zoomed in **B**, where the needle is highlighted with a blue arrow). (**C**) Trajectory of mesh electronics during non-coaxial injection to afford conformal epiretinal positioning. The concave surface of the retina with a radius of curvature of 1.5 mm is shown as the green arc, and tip of the needle loaded with mesh starts at the origin (0, 0). To ensure

conformal positioning of mesh on the curved retina surface, mesh electronics (yellow lines with increasing contrast to indicate time sequence in injection) has to be injected in a controlled, non-coaxial manner such that the top end of the mesh (indicated by red circles) needs to follow a computed trajectory (red curve) in the FoV. The pre-defined trajectory in the FoV was computed numerically with MATLAB.

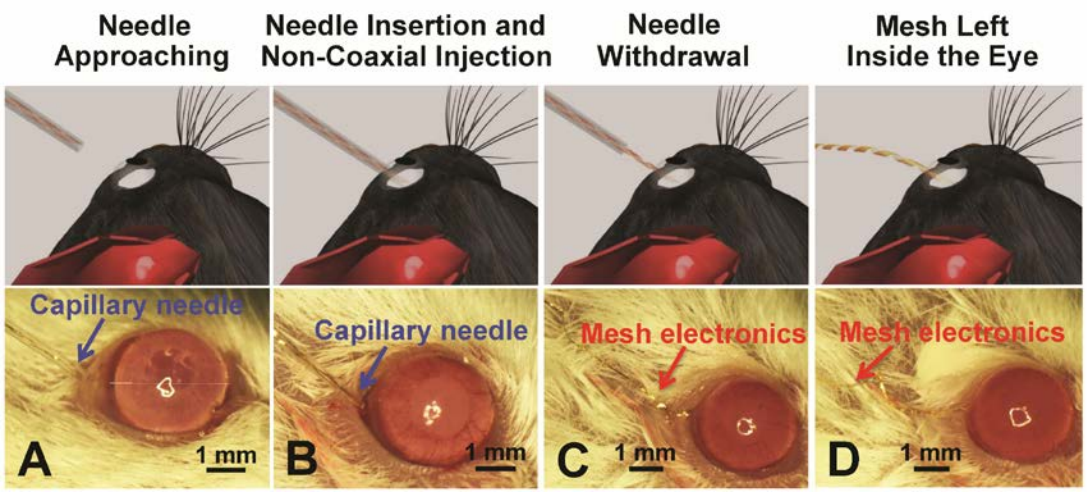

Fig. S2. In vivo non-coaxial intravitreal injection process. Schematics (top row) and corresponding photographs taken with white-light illumination and wide-field acquisition (bottom row) show the entire eye injection process, including needle approaching (**A**), needle insertion and non-coaxial injection (**B**), needle withdrawal (**C**) and mesh left inside the eye (**D**). The blue arrows indicate the glass capillary needle and the red arrows indicate the mesh electronics.

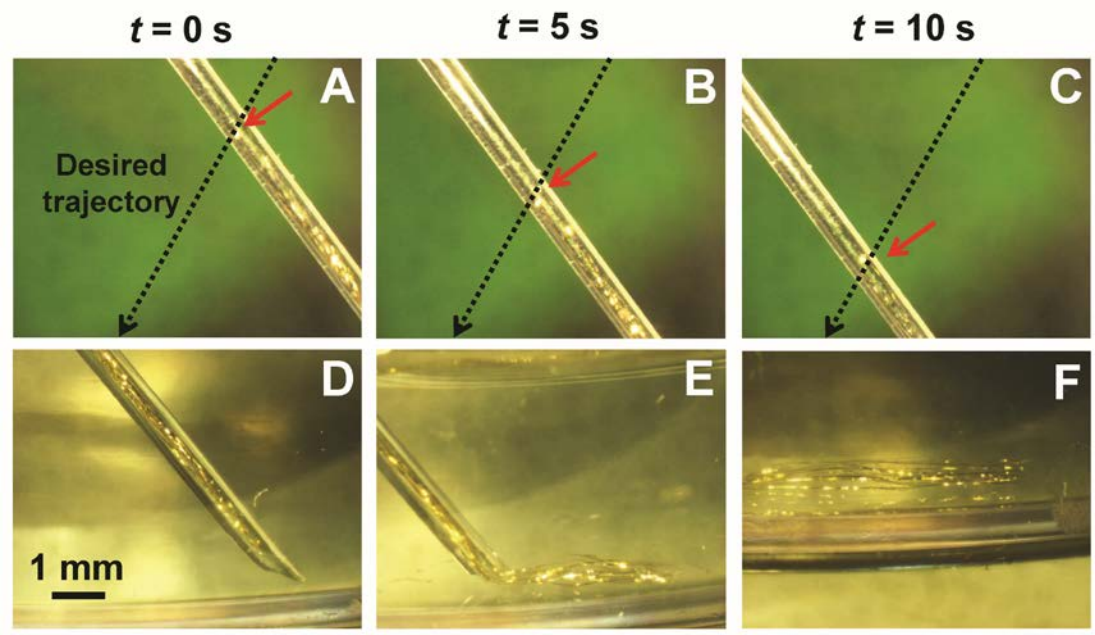

Fig. S3. Non-coaxial injection test in hydrogel. Injection test shown here was done in 0.14% hydrogel to mimic the mechanical properties of the vitreous humor of the eye (*24*), and controlled non-coaxial injection was performed by tracking the top end of the mesh (red arrows) that followed the pre-computed trajectory (black dashed line) in the FoV (**A** to **C**), while the morphology of injected mesh positioned laterally on the flat surface of a petri dish was confirmed by imaging the bottom tip of the needle (**D** to **F**). All images were taken with white-light illumination and wide-field acquisition.

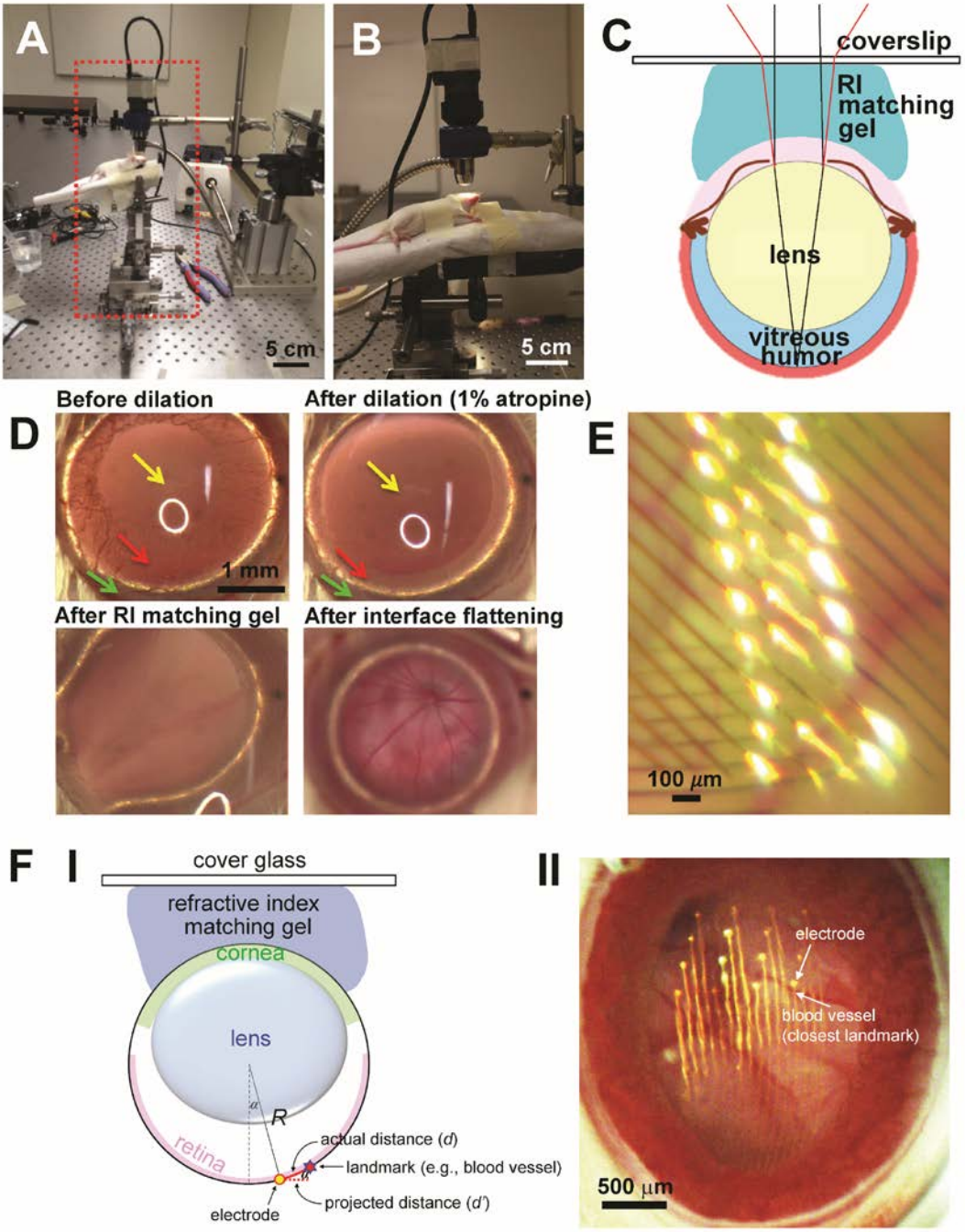

Fig. S4. Non-invasive in vivo through-lens imaging of mouse eye fundus. (**A** and **B**) White-light and wide-field photograph of the in vivo through-lens eye fundus imaging setup (**A**), with a close-up view of the red dashed box (**B**) highlighting the air gap between the objective and flattened eye lubricant gel (the 'liquid Hruby lens') by a cover slip. (**C**) Schematic showing the

construction of the ‘liquid Hruby lens’ by coating the eye with refractive index (RI) matching gel and flattening the gel/air interface with a cover slip. The black lines indicate emanating rays from an illuminated light source in the eye fundus without the ‘liquid Hruby lens’ and the red lines indicate those with the ‘liquid Hruby lens’. Note that in the case without ‘liquid Hruby lens’, the emanating rays from a point light source on the fundus appear coming from infinity due to the intrinsic focusing power of the lens, leading to difficulty in imaging the fundus with sufficient magnification. (**D**) Stepwise illustration of mouse eye fundus imaging using the ‘liquid Hruby lens’, showing the visualization of eye fundus vessels after dilation, application of RI matching gel and interface flattening. Yellow arrows: pupil; red arrows: iris; green arrows: sclera. All images were taken with white-light illumination and wide-field acquisition. (**E**) A high-resolution microscopic image with white-light illumination and wide-field acquisition, showing the close proximity between the mesh and the retina in live mouse on the same day of injection, which is indicated by the shared focal plane where both the mesh ribbons and the retinal blood vessels can be visualized (depth of focus = 20 μm). (**F**) Schematic showing the geometry used for localization of recording electrodes on the concave retina (**I**), with an example showing a pair of electrode and its closest landmark blood vessel in a real eye fundus image (**II**). α, local slope angle of an electrode and a landmark (i.e., a blood vessel) on the spherical retina surface; R, radius of the eye; d, actual distance between an electrode and its closest landmark vessel on the spherical retina surface; d', apparent distance of d from the 2D projected through-lens fundus image.

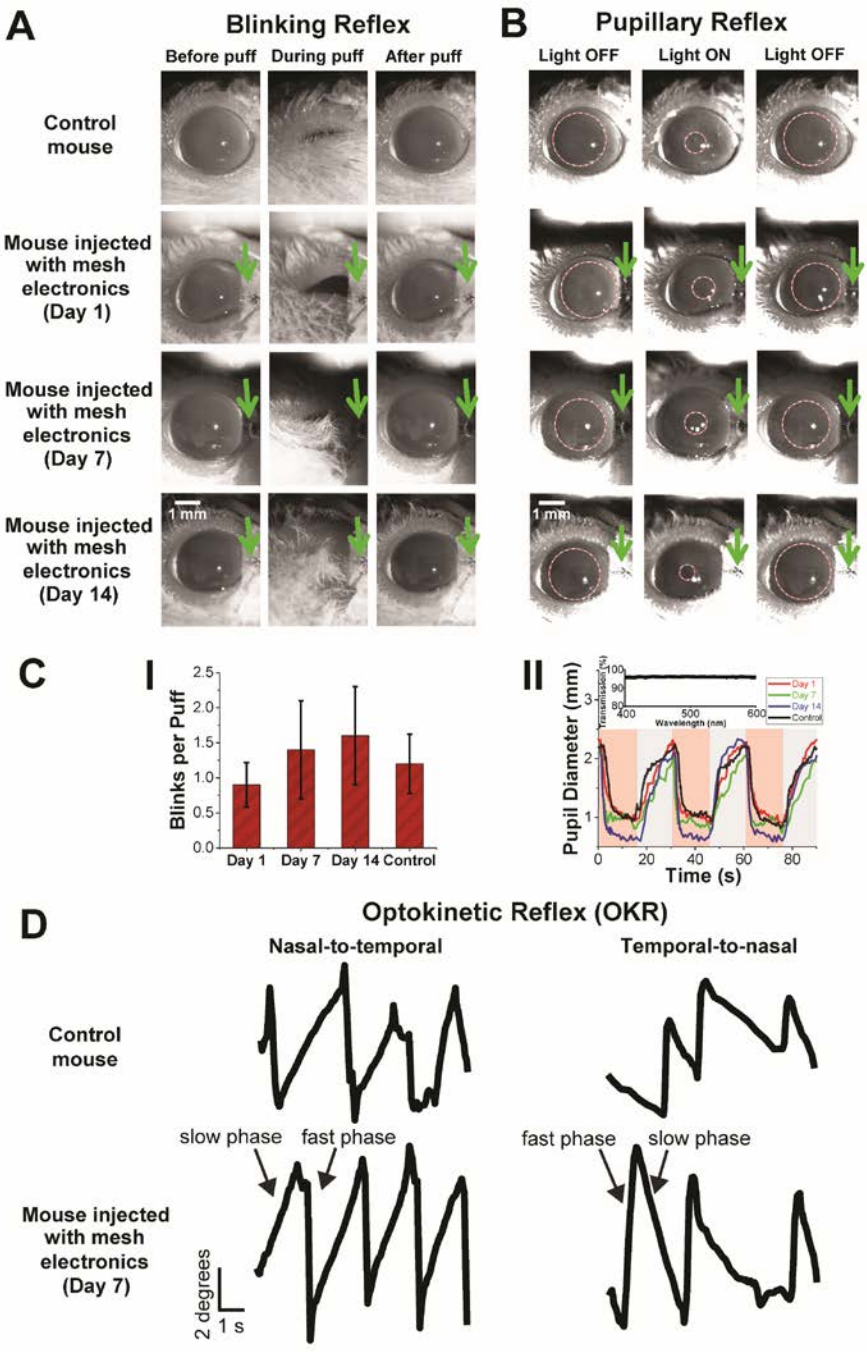

Fig. S5. Blinking, pupillary and optokinetic reflexes of mesh-injected eye. (**A**) Representative NIR images of a control mouse eye and a representative mesh-injected mouse eye on Day 1, 7 and 14 after non-surgical injection, at three different time points before, during and after the air puff was given to the eye. (**B**) Representative NIR images of the control mouse eye and the

mesh-injected mouse eye on Day 1, 7 and 14 after non-surgical injection during consecutive light OFF, ON and OFF phases. The green arrows indicate the location of injected mesh electronics in both panels (**A**) and (**B**), and the red dashed circles mark the boundary of the pupil in panel (**B**). All NIR images were taken with NIR light illumination and wide-field image acquisition. (**C**) Quantification of number of blinks per air puff (**I**) and pupil diameter change during alternating light intensity modulation (**II**) between the injected and control mouse eyes. No statistically significant difference was found between any day and the control ($P > 0.05$; $n = 10$) for blinking reflex using a one-way ANOVA test in panel (**C**), **I**. The red shaded regions indicate the 'light ON' phases while the grey shaded regions indicate the 'light OFF' phases in panel (**C**), **II**. The inset of panel (**C**), **II** shows a transmission spectrum that reveals ca. 95% light transmittance of mesh electronics in the spectral window visible to the mouse eye. (**D**) OKR eye movements produced by a control mouse eye (top) and a representative mesh-injected mouse eye on Day 7 post-injection (bottom) in response to motion in the nasal-to-temporal (left) and temporal-to-nasal (right) directions. Error bars reflect one standard deviation (±1 s.d.) in panel (**C**).

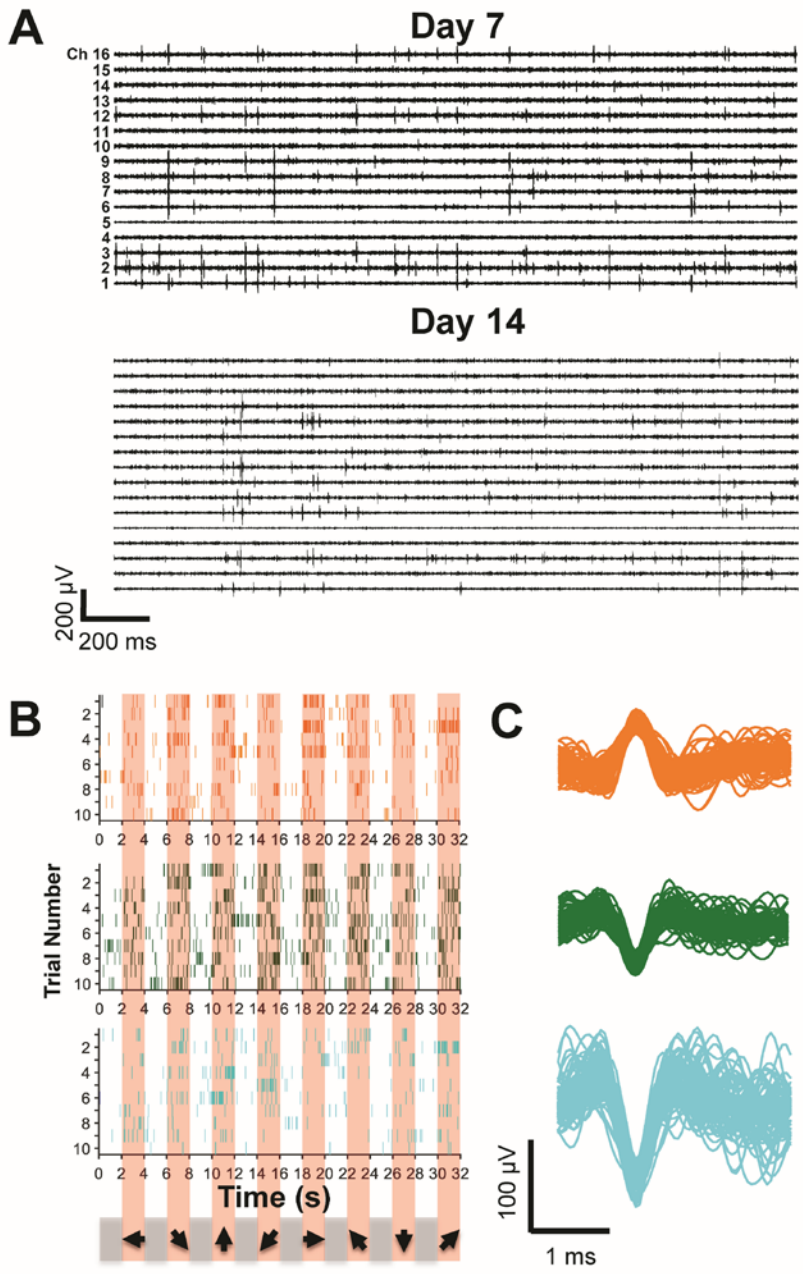

Fig. S6. Chronic 16-channel recording of DSGCs. (**A**) Representative 16-channel recordings from the same mesh electronics injected into a mouse eye on Day 7 and 14 post-injection during visual stimulation of moving gratings**.** (**B**) Raster plots of single-unit firing events of three identified neurons shown in Fig. 3 on Day 14 post-injection. (**C**) Overlaid spike waveforms of these three identified neurons on Day 14.

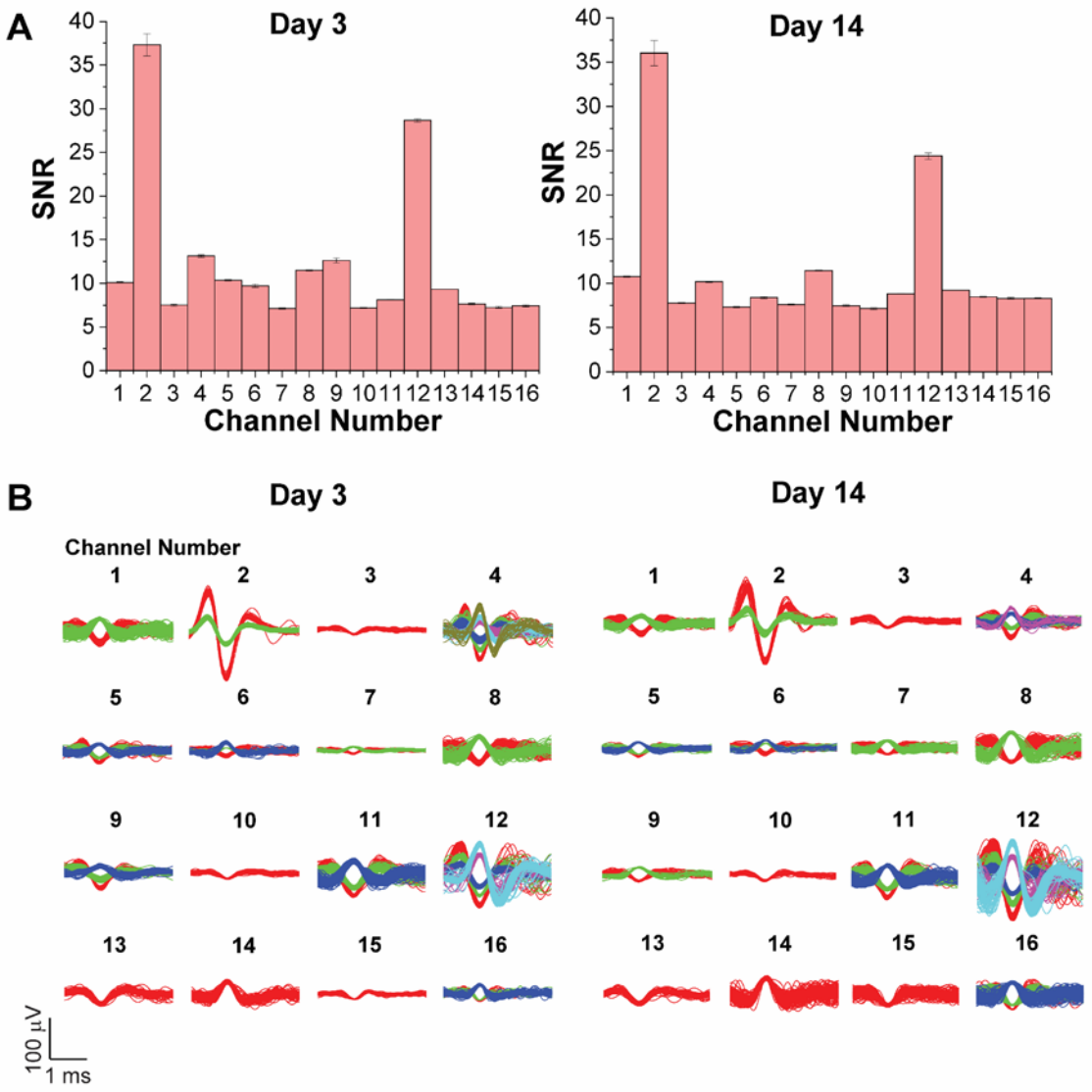

Fig. S7. Spike sorting of all 16 channels from a mesh electronics probe. (**A**) Bar charts showing average SNR of sorted single-unit spikes for all channels in a mesh electronics probe used in Fig. 2 on Day 3 and 14 post-injection. The error bars indicate ±1 s.e.m. (**B**) Overlay of sorted and clustered spikes from all channels on Day 3 and 14 post-injection.

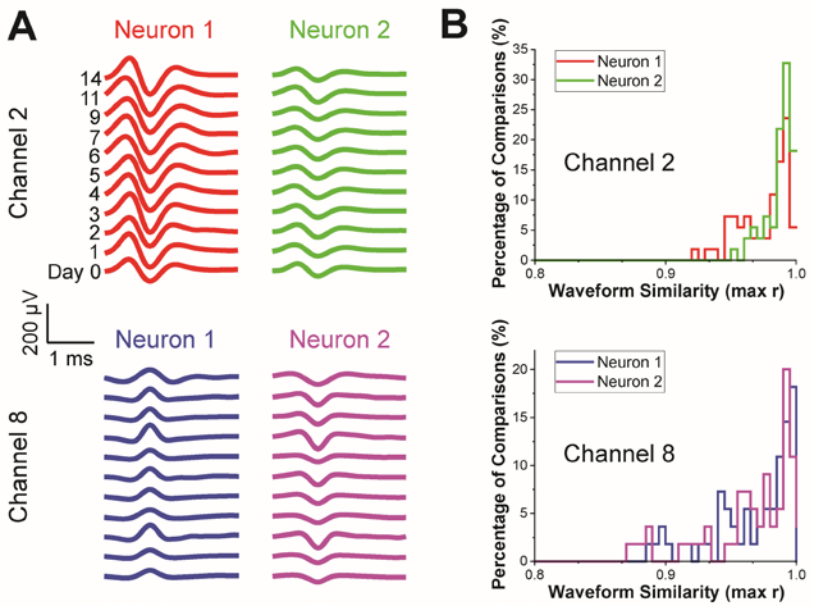

Fig. S8. Chronic spike waveform evolution over 14 days. (**A**) Average spike waveforms of two identified neurons from Ch2 (top) and two different neurons from Ch8 (bottom) of a representative mesh electronics probe used in Fig. 2, plotted for 11 different time points of recording over the course of 14 days. (**B**) Autocorrelation histograms of average waveforms of sorted spikes from 11 different time points of recording for the same neurons from Ch2 (top) and Ch8 (bottom) shown in panel (**A**).

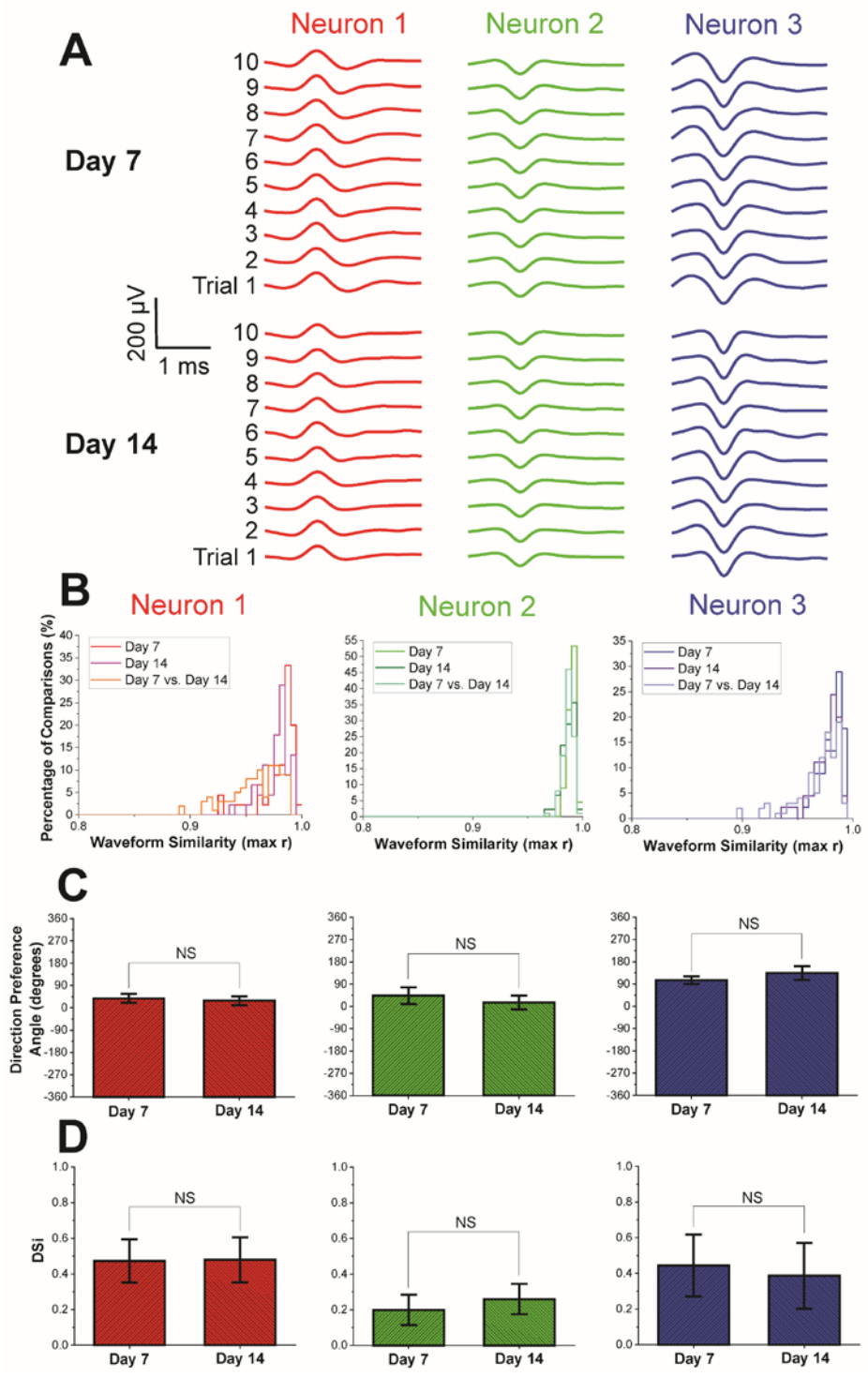

Fig. S9. Comparison of recorded spike waveforms and neural responses between different trials and between different days of trials for moving grating stimulation. (**A**) Average spike waveforms for each of 10 consecutive trials on Day 7 and 14 post-injection for three identified

neurons recorded from Ch8 of mesh electronics probe used in Fig. 3. (**B**) Same-day (Day 7 or Day 14) autocorrelation histograms between different trials and cross-day (Day 7 vs. Day 14) cross-correlation histograms between the two days for the same three neurons in panel (**A**). (**C**&**D**) Vector sum direction preference angle (**C**) and DSi (**D**) for the same three neurons in panel (**A**) between Day 7 and 14 for moving grating stimulation. NS, not significant ($P > 0.05$). Plots in panel (**C**) reveal a preference angle of neuron-1 at 0°, which is temporal, and that of neuron-3 at 90°, which is dorsal. It is noteworthy that neuron-2 also has averaged preference angle near 0°, which is a result of randomly distributed preference angles all over the angular range (from -180° to 180°), and does not imply direction selectivity due to an average DSi of <0.3 for neuron-2 in panel (**D**). The error bars indicate ±1 s.e.m. in both panels (**C**) and (**D**).

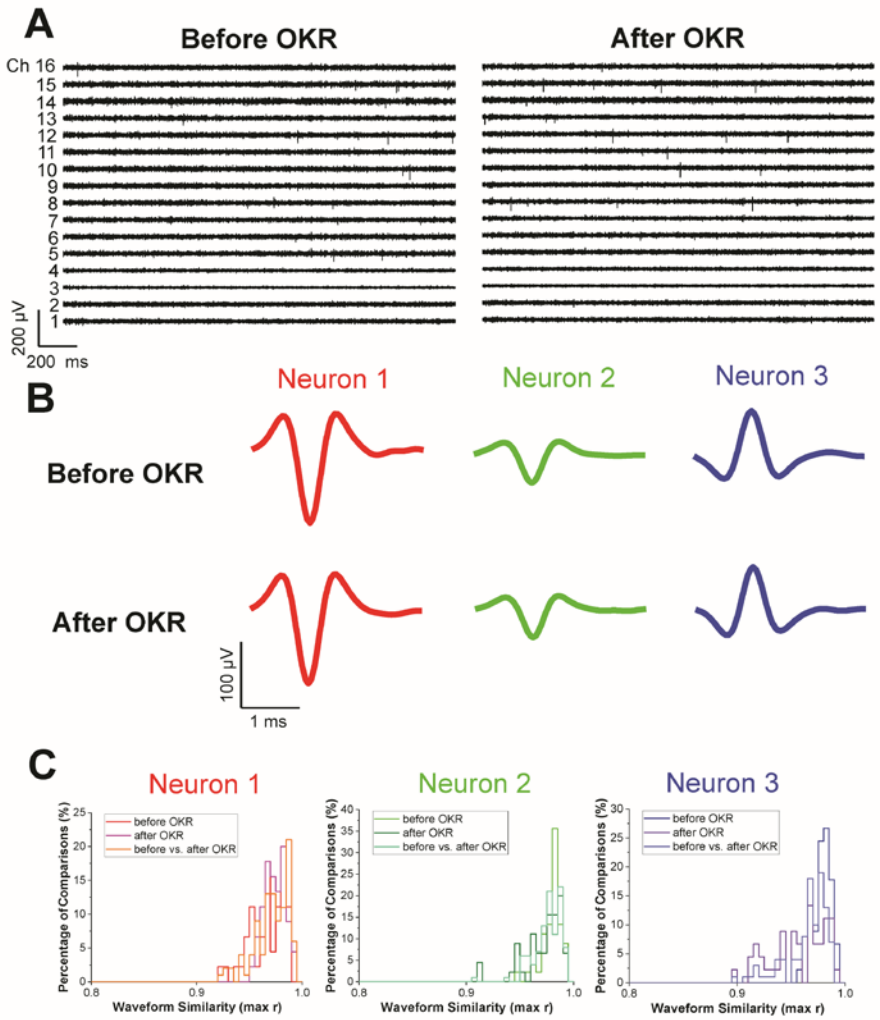

Fig. S10. Comparison of single-unit recordings before and after OKR. (**A**) Representative 16-channel recording traces before and after one OKR episode. (**B**) Average spike waveforms over a 10-s period both before and after one OKR episode for three identified neurons from a representative channel (Ch13) of the traces shown in panel (**A**). (**C**) Autocorrelation analysis for each of the 'before OKR' and 'after OKR' groups, along with cross-correlation analysis between the two groups for 10 OKR episodes.

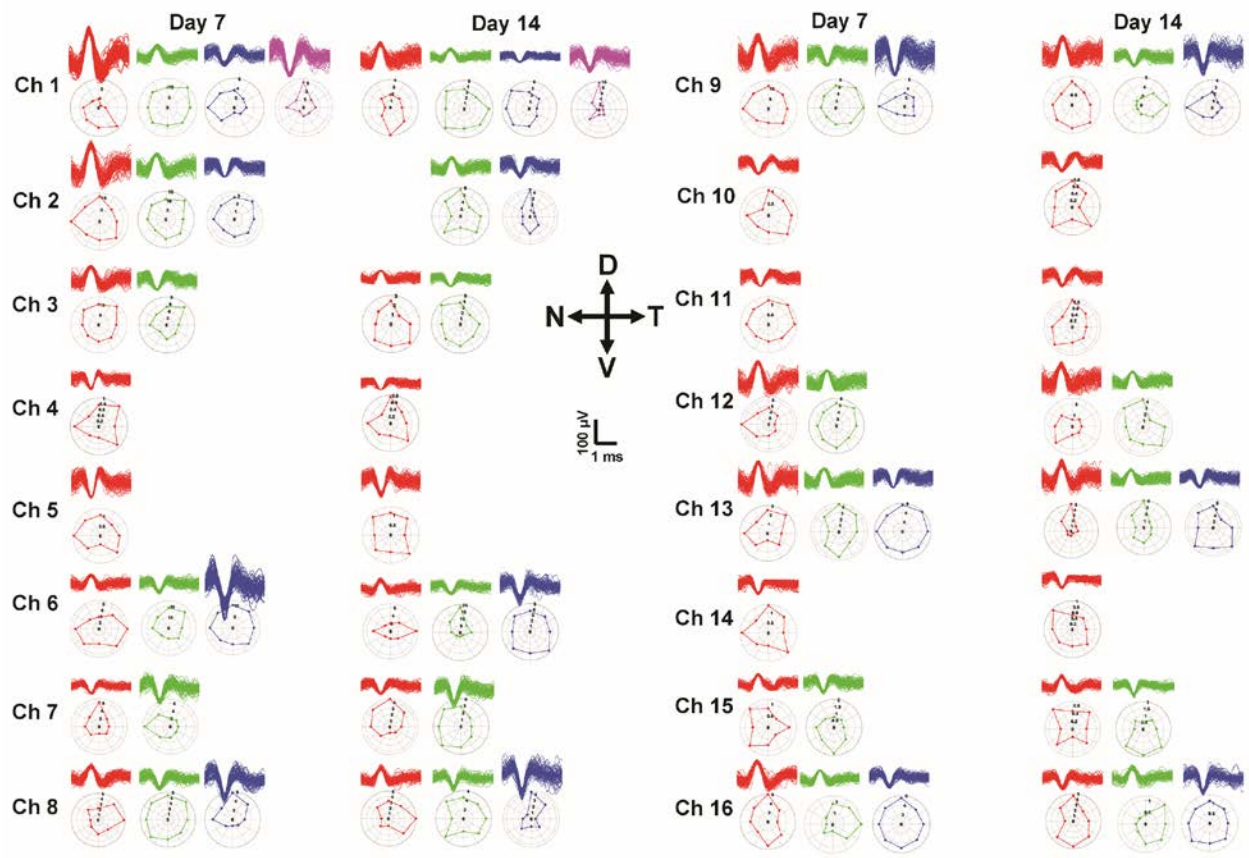

Fig. S11. Chronic recording of DSGCs, OSGCs and non-DSGCs from 16-channel mesh electronics in the same mouse eye. Overlaid spike waveforms and their corresponding polar plots are shown for all neurons (32 RGCs in total excluding those detected by multiple channels) recorded by each channel on Day 7 and Day 14 post-injection.

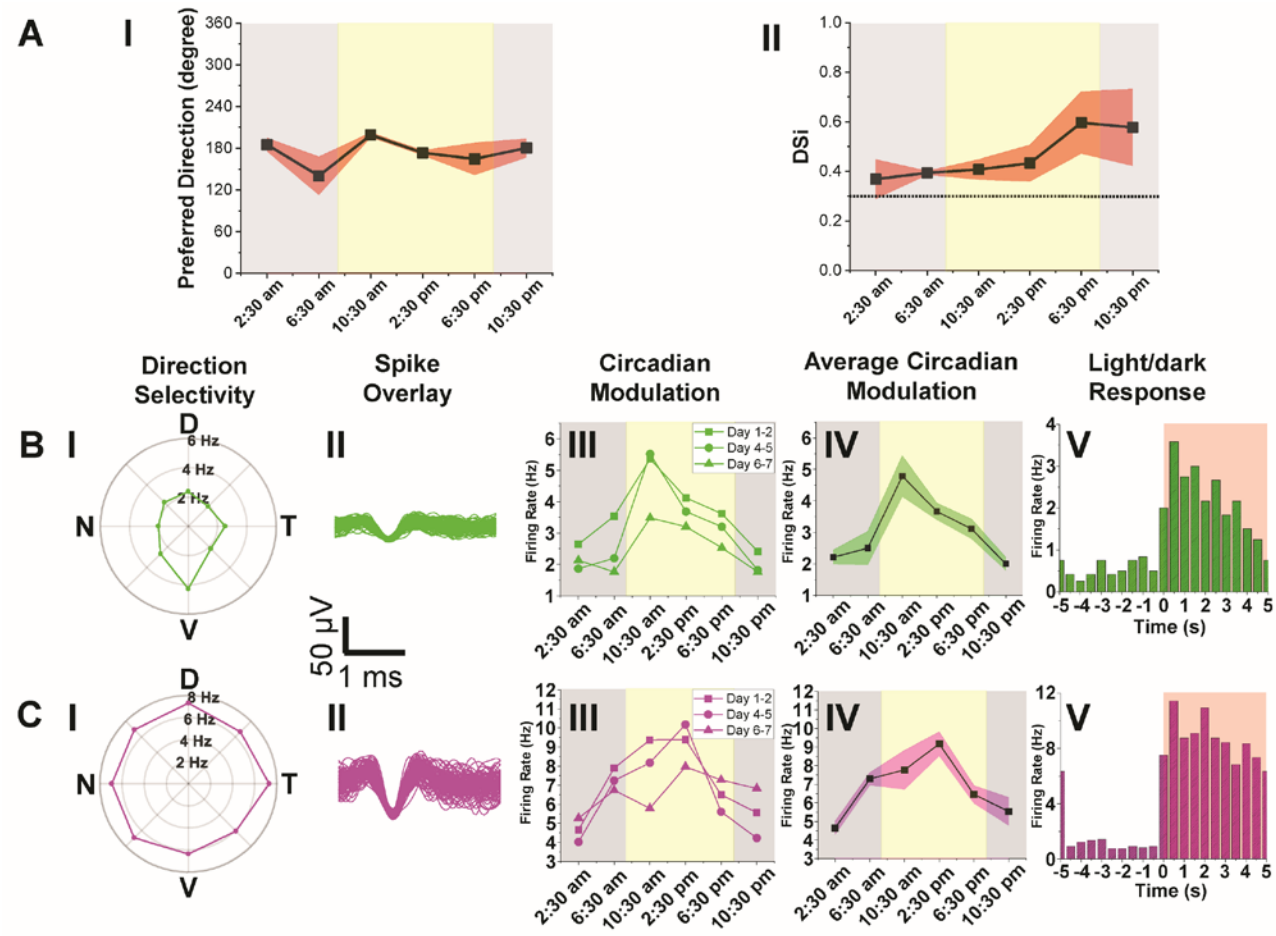

Fig. S12. Circadian modulation of RGC activity. (**A**) Evolution of preferred direction (**I**) and DSi (**II**) for a representative DSGC shown in Fig. 4, A and B, averaged over three complete circadian cycles. The horizontal dashed line in **II** represents the threshold above which RGCs are assigned DSGCs (*44*). (**B** and **C**) Polar plot showing direction selectivity (**I**), spike overlay (**II**), circadian modulation of firing rates in three complete circadian cycles on Days 1-2, 4-5 and 6-7 post-injection (**III**), average firing rate modulation over three circadian cycles (**IV**), and responses to light/dark stimulation (**V**) are shown for a DSGC (**B**) and a non-direction selective RGC (**C**). The yellow and gray shaded regions in panels (**A**), (**B**), III & IV and (**C**), III & IV indicate diurnal and nocturnal circadian times, respectively, while the red shaded and white

regions in panel **V** of both (**B**) and (**C**) indicate light ON and OFF phases, respectively. The error bars in panels (**A**), (**B**), **IV** and (**C**), **IV** indicate ±1 s.e.m.

Table S1. Distance between electrodes and closest landmarks after spherical calibration and correction on Day 0 and 14 post-injection. Electrode numbers follow the same indexing shown in Fig. 1B. The asterisk indicates the biggest distance change among all analyzed electrodes, which may be a result of deviation from small-angle approximation instead of actual positional drift as electrode 3 has the largest distance from its closest blood vessel. It is noteworthy that this drift distance marked by the asterisk is still small compared to the size of recording electrodes (20 μm).

Electrode number	**Distance on Day 0 (μm)**	**Distance on Day 14 (μm)**	**Drift distance (μm)**
Electrode 3	342.6 ± 3.4	348.5 ± 3.5	5.9 ± 4.9*
Electrode 4	75.6 ± 4.2	71.7 ± 1.3	3.9 ± 4.3
Electrode 7	159.4 ± 2.6	162.2 ± 2.1	2.8 ± 3.3
Electrode 8	119.2 ± 1.3	122.9 ± 1.7	3.7 ± 2.1

Table S2. L-ratio for each identified neuron in all 16 channels of a representative mesh electronics probe used in Fig. 2 on Day 3 and 14 post-injection. An L-ratio of < 0.05 of a specific isolated unit among all sorted spikes is considered good separation/isolation (*34*, *43*), while the L ratio is always 0 for channels where only one cluster of spikes is found.

Channel	**Neuron(s), L-ratio(s)**	
	Day 3	**Day 14**
1	N1 & N2, $<1\times10^{-6}$	N1 & N2, $<1\times10^{-6}$
2	N1 & N2, $<1\times10^{-6}$	N1 & N2, $<1\times10^{-6}$
3	N1, 0	N1, 0
4	N1, 3.49×10^{-6}; N2, 7.80×10^{-3}; N3, 5.38×10^{-4}; N4, $<1\times10^{-6}$; N5, 4.10×10^{-4}; N6, $<1\times10^{-6}$	N1, 1.48×10^{-2}; N2, $<1\times10^{-6}$; N3, 1.58×10^{-4}; N4, 9.35×10^{-5}
5	N1, 1.18×10^{-2}; N2, 7.91×10^{-5}; N3, $<1\times10^{-6}$	N1, 4.91×10^{-4}; N2, 9.46×10^{-5}; N3, $<1\times10^{-6}$
6	N1 & N2, $<1\times10^{-6}$; N3, 9.41×10^{-3}	N1 & N2, $<1\times10^{-6}$; N3, 1.75×10^{-3}
7	N1 & N2, $<1\times10^{-6}$	N1 & N2, $<1\times10^{-6}$
8	N1 & N2, $<1\times10^{-6}$	N1 & N2, $<1\times10^{-6}$
9	N1, $<1\times10^{-6}$; N2, 5.44×10^{-6}; N3, $<1\times10^{-6}$	N1 & N2, $<1\times10^{-6}$
10	N1, 0	N1, 0
11	N1, 4.29×10^{-3}; N2, 3.33×10^{-5}; N3, $<1\times10^{-6}$	N1, 2.87×10^{-2}; N2, 1.22×10^{-6}; N3, $<1\times10^{-6}$
12	N1, 2.16×10^{-6}; N2 & N3, $<1\times10^{-6}$; N4, 7.56×10^{-6}; N5, 1.41×10^{-5}	N1, 8.52×10^{-3}; N2, 1.48×10^{-3}; N3, 2.05×10^{-5}; N4, $<1\times10^{-6}$;

		N5, 1.93×10^{-5}
13	N1, 0	N1, 0
14	N1, 0	N1, 0
15	N1, 0	N1, 0
16	N1, 2.49×10^{-2}; N2, 1.09×10^{-2}; N3, $<1\times10^{-6}$	N1, 1.33×10^{-2}; N2, 2.33×10^{-4}; N3, $<1\times10^{-6}$

Movie S1. NIR pupil imaging of mouse eye injected with mesh electronics. This video shows the video-rate NIR imaging and tracking of mouse pupil size changes in response to ambient light intensity modulation. The frame rate is 25 frames per second (fps) and the video is played at 1× real time. The mesh electronics was injected and fixed to the lateral canthus of the eye (right side of the eye), and the pupil boundary is shown as the red dashed circle in the video. This video was taken on Day 1 post-injection of mesh electronics.

Movie S2. Visual stimulation with moving light gratings to a head-fixed mouse. This video shows the setup of moving grating visual stimulation to a mouse restrained in a Tailveiner® restrainer with the head-plate fixed to an optical-table-mounted frame. The frame rate is 30 frames per second (fps) and the video is played at 1× real time. This video covers the duration of gratings moving in eight different directions in one complete stimulation trial. During visual stimulation, single-neuron firing activity of RGCs is recorded through the FFC cable to external recording instrumentation and the size and central location of the pupil are tracked with a NIR camera.

References

1. R. H. Masland, The neuronal organization of the retina. *Neuron* **76**, 266–280 (2012). doi:10.1016/j.neuron.2012.10.002 Medline

2. M. Hoon, H. Okawa, L. Della Santina, R. O. Wong, Functional architecture of the retina: Development and disease. *Prog. Retin. Eye Res.* **42**, 44–84 (2014). doi:10.1016/j.preteyeres.2014.06.003 Medline

3. J. R. Sanes, R. H. Masland, The types of retinal ganglion cells: Current status and implications for neuronal classification. *Annu. Rev. Neurosci.* **38**, 221–246 (2015). doi:10.1146/annurev-neuro-071714-034120 Medline

4. T. Baden, P. Berens, K. Franke, M. Román Rosón, M. Bethge, T. Euler, The functional diversity of retinal ganglion cells in the mouse. *Nature* **529**, 345–350 (2016). doi:10.1038/nature16468 Medline

5. C. M. Lewis, C. A. Bosman, P. Fries, Recording of brain activity across spatial scales. *Curr. Opin. Neurobiol.* **32**, 68–77 (2015). doi:10.1016/j.conb.2014.12.007 Medline

6. E. J. Hamel, B. F. Grewe, J. G. Parker, M. J. Schnitzer, Cellular level brain imaging in behaving mammals: An engineering approach. *Neuron* **86**, 140–159 (2015). doi:10.1016/j.neuron.2015.03.055 Medline

7. I. J. Kim, Y. Zhang, M. Yamagata, M. Meister, J. R. Sanes, Molecular identification of a retinal cell type that responds to upward motion. *Nature* **452**, 478–482 (2008). doi:10.1038/nature06739 Medline

8. G. D. Field, J. L. Gauthier, A. Sher, M. Greschner, T. A. Machado, L. H. Jepson, J. Shlens, D. E. Gunning, K. Mathieson, W. Dabrowski, L. Paninski, A. M. Litke, E. J. Chichilnisky, Functional connectivity in the retina at the resolution of photoreceptors. *Nature* **467**, 673–677 (2010). doi:10.1038/nature09424 Medline

9. T. A. LeGates, D. C. Fernandez, S. Hattar, Light as a central modulator of circadian rhythms, sleep and affect. *Nat. Rev. Neurosci.* **15**, 443–454 (2014). doi:10.1038/nrn3743 Medline

10. K. S. Korshunov, L. J. Blakemore, P. Q. Trombley, Dopamine: A Modulator of Circadian Rhythms in the Central Nervous System. *Front. Cell. Neurosci.* **11**, 91 (2017). doi:10.3389/fncel.2017.00091 Medline

11. C. R. Jackson, G.-X. Ruan, F. Aseem, J. Abey, K. Gamble, G. Stanwood, R. D. Palmiter, P. M. Iuvone, D. G. McMahon, Retinal dopamine mediates multiple dimensions of light-adapted vision. *J. Neurosci.* **32**, 9359–9368 (2012). doi:10.1523/JNEUROSCI.0711-12.2012 Medline

12. C. K. Hwang, S. S. Chaurasia, C. R. Jackson, G. C.-K. Chan, D. R. Storm, P. M. Iuvone, Circadian rhythm of contrast sensitivity is regulated by a dopamine-neuronal PAS-

domain protein 2-adenylyl cyclase 1 signaling pathway in retinal ganglion cells. *J. Neurosci.* **33**, 14989–14997 (2013). doi:10.1523/JNEUROSCI.2039-13.2013 Medline

13. B. H. Liu, A. D. Huberman, M. Scanziani, Cortico-fugal output from visual cortex promotes plasticity of innate motor behaviour. *Nature* **538**, 383–387 (2016). doi:10.1038/nature19818 Medline

14. D. E. Wilson, D. E. Whitney, B. Scholl, D. Fitzpatrick, Orientation selectivity and the functional clustering of synaptic inputs in primary visual cortex. *Nat. Neurosci.* **19**, 1003–1009 (2016). doi:10.1038/nn.4323 Medline

15. O. S. Dhande, A. D. Huberman, Retinal ganglion cell maps in the brain: Implications for visual processing. *Curr. Opin. Neurobiol.* **24**, 133–142 (2014). doi:10.1016/j.conb.2013.08.006 Medline

16. S. W. Kuffler, Discharge patterns and functional organization of mammalian retina. *J. Neurophysiol.* **16**, 37–68 (1953). doi:10.1152/jn.1953.16.1.37 Medline

17. H. B. Barlow, R. M. Hill, W. R. Levick, Retinal Ganglion Cells Responding Selectively to Direction and Speed of Image Motion in the Rabbit. *J. Physiol.* **173**, 377–407 (1964). doi:10.1113/jphysiol.1964.sp007463 Medline

18. T.-M. Fu, G. Hong, T. Zhou, T. G. Schuhmann, R. D. Viveros, C. M. Lieber, Stable long-term chronic brain mapping at the single-neuron level. *Nat. Methods* **13**, 875–882 (2016). doi:10.1038/nmeth.3969 Medline

19. J. Liu, T.-M. Fu, Z. Cheng, G. Hong, T. Zhou, L. Jin, M. Duvvuri, Z. Jiang, P. Kruskal, C. Xie, Z. Suo, Y. Fang, C. M. Lieber, Syringe-injectable electronics. *Nat. Nanotechnol.* **10**, 629–636 (2015). doi:10.1038/nnano.2015.115 Medline

20. G. Hong, T.-M. Fu, T. Zhou, T. G. Schuhmann, J. Huang, C. M. Lieber, Syringe Injectable Electronics: Precise Targeted Delivery with Quantitative Input/Output Connectivity. *Nano Lett.* **15**, 6979–6984 (2015). doi:10.1021/acs.nanolett.5b02987 Medline

21. T. Zhou, G. Hong, T.-M. Fu, X. Yang, T. G. Schuhmann, R. D. Viveros, C. M. Lieber, Syringe-injectable mesh electronics integrate seamlessly with minimal chronic immune response in the brain. *Proc. Natl. Acad. Sci. U.S.A.* **114**, 5894–5899 (2017). doi:10.1073/pnas.1705509114 Medline

22. See supplementary materials.

23. J. J. Jun, N. A. Steinmetz, J. H. Siegle, D. J. Denman, M. Bauza, B. Barbarits, A. K. Lee, C. A. Anastassiou, A. Andrei, Ç. Aydın, M. Barbic, T. J. Blanche, V. Bonin, J. Couto, B. Dutta, S. L. Gratiy, D. A. Gutnisky, M. Häusser, B. Karsh, P. Ledochowitsch, C. M. Lopez, C. Mitelut, S. Musa, M. Okun, M. Pachitariu, J. Putzeys, P. D. Rich, C. Rossant, W. L. Sun, K. Svoboda, M. Carandini, K. D. Harris, C. Koch, J. O'Keefe, T. D. Harris,

Fully integrated silicon probes for high-density recording of neural activity. *Nature* **551**, 232–236 (2017). doi:10.1038/nature24636 Medline

24. C. S. Nickerson, H. L. Karageozian, J. Park, J. A. Kornfield, The mechanical properties of the vitreous humor. *Invest. Ophthalmol. Vis. Sci.* **45**, 37 (2004).

25. X. Duan, M. Qiao, F. Bei, I.-J. Kim, Z. He, J. R. Sanes, Subtype-specific regeneration of retinal ganglion cells following axotomy: Effects of osteopontin and mTOR signaling. *Neuron* **85**, 1244–1256 (2015). doi:10.1016/j.neuron.2015.02.017 Medline

26. I. J. Kim, Y. Zhang, M. Meister, J. R. Sanes, Laminar restriction of retinal ganglion cell dendrites and axons: Subtype-specific developmental patterns revealed with transgenic markers. *J. Neurosci.* **30**, 1452–1462 (2010). doi:10.1523/JNEUROSCI.4779-09.2010 Medline

27. Y. Zhang, I. J. Kim, J. R. Sanes, M. Meister, The most numerous ganglion cell type of the mouse retina is a selective feature detector. *Proc. Natl. Acad. Sci. U.S.A.* **109**, E2391–E2398 (2012). doi:10.1073/pnas.1211547109 Medline

28. N. Suematsu, T. Naito, T. Miyoshi, H. Sawai, H. Sato, Spatiotemporal receptive field structures in retinogeniculate connections of cat. *Front. Syst. Neurosci.* **7**, 103 (2013). doi:10.3389/fnsys.2013.00103 Medline

29. D. Zoccolan, B. J. Graham, D. D. Cox, A self-calibrating, camera-based eye tracker for the recording of rodent eye movements. *Front. Neurosci.* **4**, 193 (2010). doi:10.3389/fnins.2010.00193 Medline

30. K. Yonehara, M. Fiscella, A. Drinnenberg, F. Esposti, S. Trenholm, J. Krol, F. Franke, B. G. Scherf, A. Kusnyerik, J. Müller, A. Szabo, J. Jüttner, F. Cordoba, A. P. Reddy, J. Németh, Z. Z. Nagy, F. Munier, A. Hierlemann, B. Roska, Congenital Nystagmus Gene FRMD7 Is Necessary for Establishing a Neuronal Circuit Asymmetry for Direction Selectivity. *Neuron* **89**, 177–193 (2016). doi:10.1016/j.neuron.2015.11.032 Medline

31. G. T. Prusky, N. M. Alam, S. Beekman, R. M. Douglas, Rapid quantification of adult and developing mouse spatial vision using a virtual optomotor system. *Invest. Ophthalmol. Vis. Sci.* **45**, 4611–4616 (2004). doi:10.1167/iovs.04-0541 Medline

32. G. H. Jacobs, G. A. Williams, H. Cahill, J. Nathans, Emergence of novel color vision in mice engineered to express a human cone photopigment. *Science* **315**, 1723–1725 (2007). doi:10.1126/science.1138838 Medline

33. R. Q. Quiroga, Z. Nadasdy, Y. Ben-Shaul, Unsupervised spike detection and sorting with wavelets and superparamagnetic clustering. *Neural Comput.* **16**, 1661–1687 (2004). doi:10.1162/089976604774201631 Medline

34. N. Schmitzer-Torbert, A. D. Redish, Neuronal activity in the rodent dorsal striatum in sequential navigation: Separation of spatial and reward responses on the multiple T task. *J. Neurophysiol.* **91**, 2259–2272 (2004). doi:10.1152/jn.00687.2003 Medline

35. A. Jackson, E. E. Fetz, Compact movable microwire array for long-term chronic unit recording in cerebral cortex of primates. *J. Neurophysiol.* **98**, 3109–3118 (2007). doi:10.1152/jn.00569.2007 Medline

36. W. Sun, Z. Tan, B. D. Mensh, N. Ji, Thalamus provides layer 4 of primary visual cortex with orientation- and direction-tuned inputs. *Nat. Neurosci.* **19**, 308–315 (2016). doi:10.1038/nn.4196 Medline

37. L. Gurevich, M. M. Slaughter, Comparison of the waveforms of the ON bipolar neuron and the b-wave of the electroretinogram. *Vision Res.* **33**, 2431–2435 (1993). doi:10.1016/0042-6989(93)90122-D Medline

38. T.-M. Fu, G. Hong, R. D. Viveros, T. Zhou, C. M. Lieber, Highly scalable multichannel mesh electronics for stable chronic brain electrophysiology. *Proc. Natl. Acad. Sci. U.S.A.* **114**, E10046–E10055 (2017). doi:10.1073/pnas.1717695114 Medline

39. Z. Xie, F. Chen, X. Wu, C. Zhuang, J. Zhu, J. Wang, H. Ji, Y. Wang, X. Hua, Safety and efficacy of intravitreal injection of recombinant erythropoietin for protection of photoreceptor cells in a rat model of retinal detachment. *Eye* **26**, 144–152 (2012). doi:10.1038/eye.2011.254 Medline

40. K. Hruby, Slit lamp microscopy of the posterior section of the eye with the new preset lens. *Arch. Ophthalmol.* **43**, 330–336 (1950). doi:10.1001/archopht.1950.00910010337010 Medline

41. S. Thompson, S. F. Stasheff, J. Hernandez, E. Nylen, J. S. East, R. H. Kardon, L. H. Pinto, R. F. Mullins, E. M. Stone, Different inner retinal pathways mediate rod-cone input in irradiance detection for the pupillary light reflex and regulation of behavioral state in mice. *Invest. Ophthalmol. Vis. Sci.* **52**, 618–623 (2011). doi:10.1167/iovs.10-6146 Medline

42. I. L. Jones, T. L. Russell, K. Farrow, M. Fiscella, F. Franke, J. Müller, D. Jäckel, A. Hierlemann, A method for electrophysiological characterization of hamster retinal ganglion cells using a high-density CMOS microelectrode array. *Front. Neurosci.* **9**, 360 (2015). doi:10.3389/fnins.2015.00360 Medline

43. N. Schmitzer-Torbert, J. Jackson, D. Henze, K. Harris, A. D. Redish, Quantitative measures of cluster quality for use in extracellular recordings. *Neuroscience* **131**, 1–11 (2005). doi:10.1016/j.neuroscience.2004.09.066 Medline

44. S. Kondo, K. Ohki, Laminar differences in the orientation selectivity of geniculate afferents in mouse primary visual cortex. *Nat. Neurosci.* **19**, 316–319 (2016). doi:10.1038/nn.4215 Medline